A-11

NASA CONTRACTOR REPORT

NASA CR-84

NASA CR-84

AMPTIAC

EXTREME VACUUM TECHNOLOGY (BELOW 10^{-13} TORR) AND ASSOCIATED CLEAN SURFACE STUDIES

by Paul J. Bryant, Charles M. Gosselin, and Lyle H. Taylor

20020326 082

NATIONAL AERONAUTICS AND SPACE ADMINISTRATION • WASHINGTON, D. C. • JULY 1964

EXTREME VACUUM TECHNOLOGY (BELOW 10^{-13} TORR)

AND ASSOCIATED CLEAN SURFACE STUDIES

By Paul J. Bryant, Charles M. Gosselin,
and Lyle H. Taylor

NATIONAL AERONAUTICS AND SPACE ADMINISTRATION

TABLE OF CONTENTS

TABLE OF CONTENTS (Continued)

List of Figures

TABLE OF CONTENTS (Continued)

List of Figures (Continued)

TABLE OF CONTENTS (Concluded)

List of Figures (Concluded)

List of Tables

SUMMARY

The experimental work on this program was grouped under five
phases as follows:

I. Development of Extreme Vacuum Technology Utilizing the Vapor-Jet Mechanism
and a Helium Permeation Guard Technique

   A. A helium guard technique for glass was developed which lowers
the permeation of helium by three orders of magnitude. The technique which con-
sists of treatment with cesium metal may be easily applied to existing glass
systems.

   After the cesiation treatment, the pressure in a special glass system
using five stages of mercury vapor pumping, fell below the detectable level of a
commercial Redhead magnetron gauge (10^{-13} Torr or below).

   B. A special vapor-jet test system was designed and operated to ana-
lyze experimental jet designs. Results indicate that both the pump speed and
the pressure differential across a jet vary directly with boiler pressure; how-
ever, pump speed reaches a peak and falls off long before the maximum pressure
differential is reached. Thus, a two boiler or combination jet arrangement is
indicated.

II. Determination of the Quantities and Species of Gas Above Getter-ion Pumps
and Chemically-Trapped Oil Diffusion Pumps

   The spectrum of gases above a getter-ion pump was recorded. The re-
sults indicate that this type pump has a limited ability to remove helium, i.e.,
pump surfaces eventually become saturated. However, it was also shown that
these surfaces can be reactivated by a 455°C bake in vacuum.

   The gases above a chemically-trapped oil (DC-705) diffusion pump have
been studied by means of a sensitive partial pressure analyzer. It has been
shown that no oil components can be detected in the system if the chemical trap
is at liquid nitrogen temperature; however, trace amounts are detectable if the
trap is at room temperature. A discussion of the other gases present is given.

- 1 -

III. A Physical Adsorption Isotherm for Inert Gases

The performance of a cryogenic vacuum system depends on the amount of gas a cryopanel can adsorb, i.e., on the adsorption isotherm. A new physical adsorption isotherm based on a triangular site model has been derived. This isotherm is linear for very low coverages, reduces to the Langmiur adsorption isotherm when there is only first layer coverage, yields a superposition of two Langmiur adsorption isotherms when there are only two layers present, exhibits distinctive steps as each additional layer is condensed, and predicts finite film thicknesses for saturation pressures. The complex equations, which must (for three layers or more) be solved iteratively, have been programmed and executed on an IBM 1620 Data Processing System. Results have been obtained for helium, hydrogen, and neon gases being adsorbed on porous glass at 4.28° and 8.00°K. These results vividly demonstrate how the theory can be used to economically design future cryopanels for specific jobs.

IV. Development of a Total-Pressure Gauge for Readings Below 10^{-12} Torr

Development work with total-pressure gauges was carried out with commercial Redhead magnetron gauges (NRC type 552). The ion current-to-gas pressure response for helium was found to break sharply from linearity at 7×10^{-10} Torr (or 4×10^{-9} Torr when corrected for the low ionization sensitivity of helium). A plot of the response for pressures below the break assumed a slope of 1.43 so that an indicated reading of 1×10^{-13} Torr for helium should be corrected to 1.3×10^{-12} Torr due to the nonlinear response and to 8.4×10^{-12} Torr due to the low ionization sensitivity of helium.

Following a cesiation treatment of the gauge elements, the sensitivity increased by a factor of two and the break point moved down by a factor of two. Another beneficial result of the cesium treatment technique was the instantaneous striking ability afforded even at the lowest pressures. The extreme high vacuum system used for this gauge development program took the ion current response to a value below the detectable limit with the present equipment. Further development of the magnetron gauge is now indicated.

V. Investigation of the Adhesion of Metals Exposed to Vacuum and Thermal Outgassing $p\,6l \longrightarrow$

The adhesion or cold welding tendency of structural metals as a result of vacuum and thermal outgassing was investigated. Stainless steel, aluminum, and titanium alloys were exposed to a UHV of 3×10^{-10} Torr for 1,000 hr. and to a 350°C thermal degassing treatment in a 10^{-8} Torr vacuum for 100 hr.

Samples were tested with both the original surface texture and with polished surfaces. The sample faces were exposed for vacuum degassing, then brought into contact by rotating the vacuum system. The maximum angle of repose between the samples under the influence of gravity gave a measure of adhesion. The angle of repose was less for polished samples, but no change occurred due to either vacuum exposure or combined thermal and vacuum outgassing.

The surface energy criterion for cold welding predicts a welding between two surfaces when the formation of a common interface results in a lowering of the net free surface energy of the two materials. Therefore, metal surfaces with stable oxide layers would not be expected to cold weld according to this criterion as the experimental results have verified.

I. DEVELOPMENT OF EXTREME VACUUM TECHNOLOGY UTILIZING THE VAPOR-JET MECHANISM AND A HELIUM PERMEATION GUARD TECHNIQUE

The ultimate vacuum in a room temperature glass chamber is limited by helium permeation[1] from the atmosphere through the glass walls. A simple technique has been developed which lowers the room temperature permeation rate by three orders of magnitude (see Section A below).

The ultimate vacuum in a mercury diffusion pumped system may also be limited by the back diffusion of gases through the vapor jets.[1] A special vapor-jet test system was used to predict an improved design arrangement for reducing back diffusion, without the attendant loss of pumping speed (see Section B).

A. A Technique for Reducing Helium Permeation Through Glass

A simple method for treating glass vacuum chambers to significantly reduce the helium permeation rate has been discovered. The treatment may be applied to existing vacuum systems by merely introducing a few granules of cesium nitrate into the system then baking to about 425°C. The cesium nitrate compound decomposes above 414°C and free cesium metal is evolved. Cesium is a proper replacement for silicon in the silicon dioxide tetrahedra of glass. Cesium is very active chemically and the possible combinations with a clean glass surface are many. Several forms of cesium oxide with temperature stability to 400°C are known. Such a cesium treatment was applied to two large glass vacuum systems and was found to lower the ultimate pressure limit and the partial pressure content of helium. The partial pressure analyzer system (see Section II) was used to determine the effect of cesium treatment upon a large pyrex glass re-entrant tube (Fig. 1). Introduction of a full atmosphere of helium (760 Torr) failed to raise the helium level in the analyzer. The same experiment applied to the same glass tube before cesium treatment increased the helium partial pressure by a factor of three.

Two additional experiments were performed with vycor glass helium diffusers. One was attached to the partial pressure analyzer and treated with cesium. The other vycor diffuser was attached to the extreme high vacuum system and treated with cesium. In both systems the normal operation of the diffuser was found to be reduced by three orders of magnitude at moderate temperatures. By raising the vycor diffuser to approximately 325°C the cesium treatment can be removed and subsequent operation is again normal.

The ease with which this simple treatment may be added or removed and the significant reduction afforded give promise of wide application to glass vacuum systems.

- 4 -

TO He SOURCE

TO PARTIAL
PRESSURE
ANALYZER
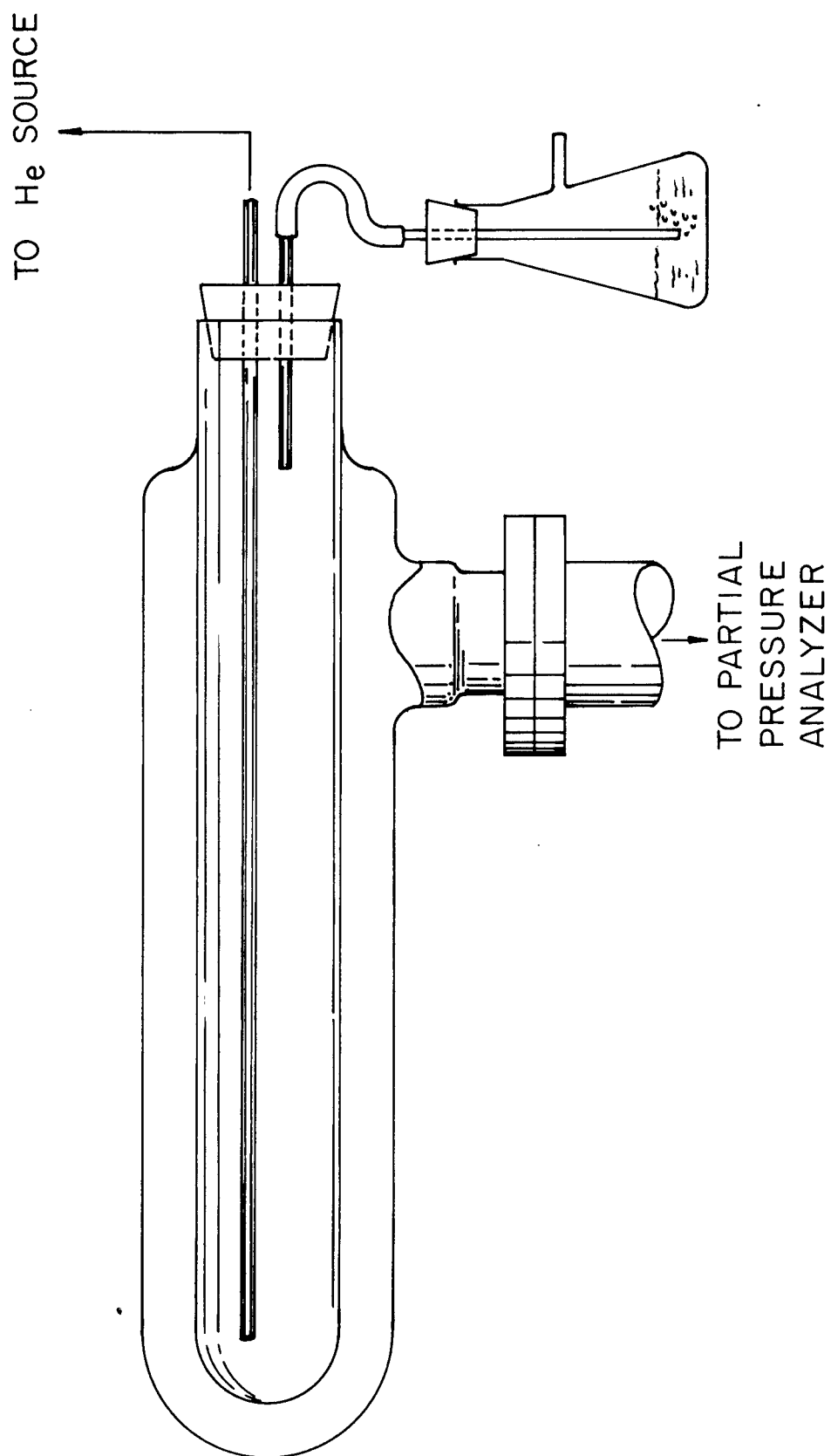
Fig. 1 - Schematic of Helium Permeation Test Apparatus

B. Analysis and Development of the Vapor-Jet Pumping Mechanism

The vapor-jet pumping mechanism is a useful tool for obtaining an ultra-high vacuum.[1,2] However, there are serious limitations which become prominent in the UHV range, namely: back diffusion, back spraying, and the production of gases from pump components (including pumping fluid). The purpose of this phase of the program is to study these effects and to suggest improved diffusion pump designs.

A vapor-jet test system (see Fig. 2) has been designed, constructed, and tested in which the effects of vapor pumping and back diffusion can be studied as functions of the operating parameters, i.e., boiler pressure,[3-5] wall temperature,[3-5] nozzle geometry,[3-6] and stack geometries. The results of these variations can then be evaluated in terms of (1) pump speed,[3] (2) pressure differences which can be maintained across a pumping stage (pressure differentials),[7] and (3) vapor-jet configurations.[4,8] This chamber has been designed to permit not only dynamical pump speed and pressure differential measurements, but also photographic studies by use of a glow discharge technique.[8]

1. Design of vapor-jet test system: The pump speed measuring subsystem is shown schematically in Fig. 3. Helium or H_2 can be diffused into the vapor-jet test chamber through a calibrated conductance, C. The pressures on each side of this calibrated orifice are measured by Bayard Alpert gauges (B.A.G. 1 and B.A.G. 2). The throughput of gas is therefore given by the equation:

$$Q = C(P_2-P_1) \, ,$$

where Q = quantity of gas (Torr liters sec.$^{-1}$) ,

   C = conductance (liters sec.$^{-1}$) ,

   P = pressure (Torr) .
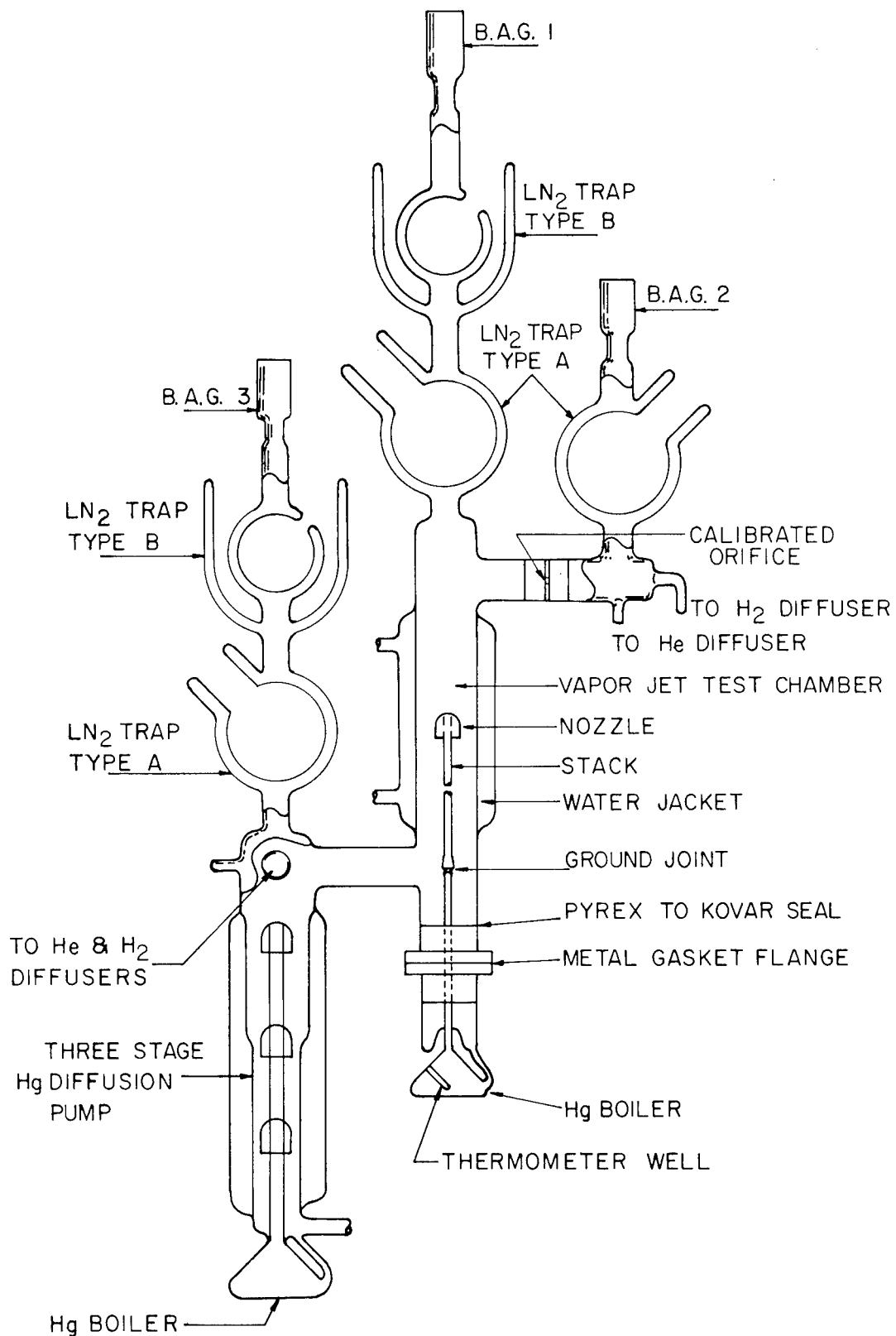
Fig. 2 - Schematic of Main Glass Apparatus of the Vapor-Jet Test System
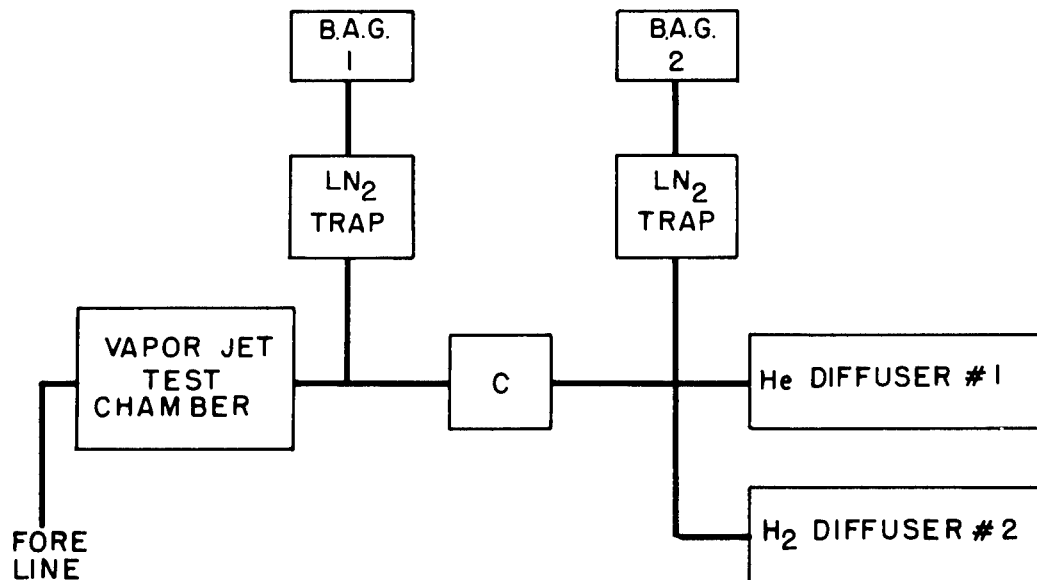
Fig. 3 - Schematic of the Pump Speed Measuring System. He or H_2 May be Leaked
Into the Test Chamber Through the Diffuser No. 1 and No. 2 and the
Calibrated Conductance, C . Pressure Indication of B.A.G. 1
and B.A.G. 2 Permits Calculation of the Throughput.
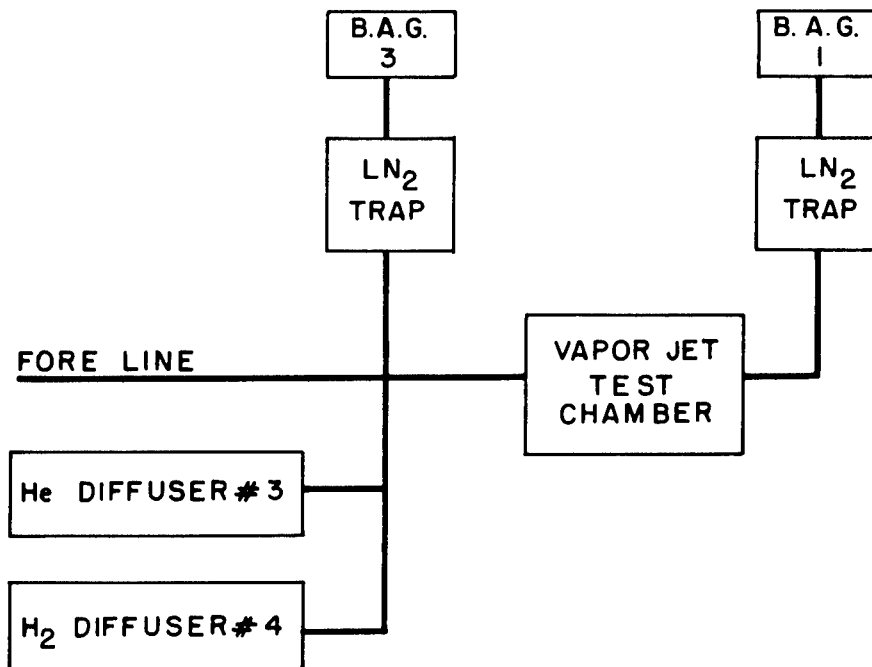
Fig. 4 - Schematic of the Pressure Differential Measuring Subsystem. He or H_2
May be Introduced Into the Foreline by Diffuser No. 3 or No. 4.
Pressure Indications of B.A.G. 3 and B.A.G. 1 Then Give
The Pressure Difference Across the Test Chamber.

When B.A.G. 1 and B.A.G. 2 indicate that an equilibrium pressure ratio has been established, the pumping speed is given by:

$$S_p = \frac{Q}{P_1}$$

where S_p = pump speed (liters sec.$^{-1}$) ,

     Q = throughput (Torr liters sec.$^{-1}$) ,

     P_1 = pressure indicated by B.A.G. 1 .

Note that by the use of a LN_2 trap the system measures essentially the pumping characteristics for the two noncondensible gases (He, H_2) which are being added to the system by means of the diffusers No. 1 and No. 2.

Pressure differential measurements can be made by using the sub-system as shown schematically in Fig. 4. Helium and H_2 may be introduced into the foreline by means of diffusers No. 3 and No. 4. Therefore the concentration of He and H_2 can be raised in the forepressure line and can be monitored by B.A.G. 3 . Pressure changes indicated by B.A.G. 1 will give a qualitative indication of back diffusion from the foreline.

A "glow discharge" technique was developed to render the pumping fluid (mercury) visible and to thus study vapor stream characteristics. The glow discharge in the mercury gas is achieved by using a high frequency generator (tesla coil) connected to a circular electrode (5 in. O.D. x 1 in. wide) encompassing the water jacket of the test region. This technique is useful for determining the envelope geometry and expansion ratios of various vapor jet designs.

2. Construction of vapor-jet test system: The main glass system (Fig. 2) consists of an experimental diffusion pump which operates in the UHV range by virtue of a standard three-stage pump used as a backing pump. Various jet designs may be inserted in the experimental chamber by means of a removable boiler. The system components are briefly described below.

The 75 liter/sec three-stage glass mercury diffusion pump, which is used as a backing pump, has a 75 mm. I.D. inlet. It is connected to the test chamber via a 60 mm. I.D. glass tube. The test chamber is actually an experimental diffusion pump consisting of a 60 mm. I.D. test chamber equipped with a cooling jacket and a demountable boiler-jet assembly. The high vacuum end of

the test chamber is connected by means of a 35 mm. I.D. glass tube to a trap-gauge assembly·and by means of a 60 mm. I.D. tube to a known conductance orifice.

The calibrated orifice was made by accurately boring a small hole, with an ultrasonic drill, through a glass plate of known thickness. To bore the orifice, a 1/8 in. diameter brass tip was mounted on an ultrasonic drilling cone. An optical grit (120) was used as the abrasive in a water suspension. Chipping around the edge of the orifice was minimized by drilling from each surface to the center of the plate. The walls of the orifice were then polished with a 400 grit paste on a ceramic rod at rotational speeds varying from 1,000 - 16,000 rpm. The thickness and diameter of the orifice were then measured accurately. The dimensions of the orifice are 0.433 ± 0.012 cm. diameter by 0.323 ± 0.012 cm. length.

The conductance (F) of the orifice was calculated by a standard equation[9] for the free molecule flow pressure range

$$ F = 3.638 \ KA \left(\frac{T}{M} \right)^{1/2} (\text{liters/sec}) \ , $$

where   K = Clausing or variational factor ,

A = Cross-sectional area of the orifice (cm.^2) ,

T = Temperature (°K) , and

M = Gram molecular weight of gas species .

The constant 3.638 carries the dimensions necessary to give $[F]$ in liters per second. Conductance values for various gases were computed using the Clausing factors, as given by Dushman.[9] The results for He, O_2, and Hg are shown in Table I for temperatures covering the operational range from below room up to bake-out.

TABLE I

CALCULATION OF ORIFICE CONDUCTANCE

K = 0.5814   A = 0.1480

He M = 4.0026		O₂ M = 31.9988		Hg M = 200.5900	
Temp. (°K)	F (liters/sec)	Temp. (°K)	F (liters/sec)	Temp. (°K)	F (liters/sec)
250.00	2.47	250.00	0.87	250.00	0.34
275.00	2.59	275.00	0.91	275.00	0.36
300.00	2.71	300.00	0.95	300.00	0.38
325.00	2.82	325.00	0.99	325.00	0.39
350.00	2.92	350.00	1.03	350.00	0.41
375.00	3.03	375.00	1.07	375.00	0.42
400.00	3.12	400.00	1.10	400.00	0.44
425.00	3.22	425.00	1.14	425.00	0.45
450.00	3.31	450.00	1.17	450.00	0.46
475.00	3.41	475.00	1.20	475.00	0.48
500.00	3.49	500.00	1.23	500.00	0.49
525.00	3.58	525.00	1.26	525.00	0.50
550.00	3.67	550.00	1.29	550.00	0.51
575.00	3.75	575.00	1.32	575.00	0.53
600.00	3.83	600.00	1.35	600.00	0.54
625.00	3.91	625.00	1.38	625.00	0.55
650.00	3.98	650.00	1.41	650.00	0.56
675.00	4.06	675.00	1.43	675.00	0.57
700.00	4.14	700.00	1.46	700.00	0.58

The boiler unit for the experimental diffusion pump is mounted on a
60 mm. I.D. glass-to-Kovar seal, with a stainless steel flange (Varian 4-1/2 in.
x 2-1/2 in. Conflat flange). A similar flange has also been attached to the
bottom end of the test chamber. An ultra-high vacuum seal can be maintained
for at least two months with a standard disposable copper gasket between the
flange faces. Experience has shown that mercury amalgamation is limited to the
inner edge of the disposable gasket. The removable jet stack is a 12.5 mm. I.D.
glass tube mounted on a ground glass joint. At the other end of the stack the
experimental nozzle assemblies can be mounted. Figure 5 shows the boiler assem-
bly jet stack, and an experimental nozzle assembly. Note that the experimental
diffusion pump boiler is fitted with a re-entrant tube for the insertion of
temperature sensors.

(b)
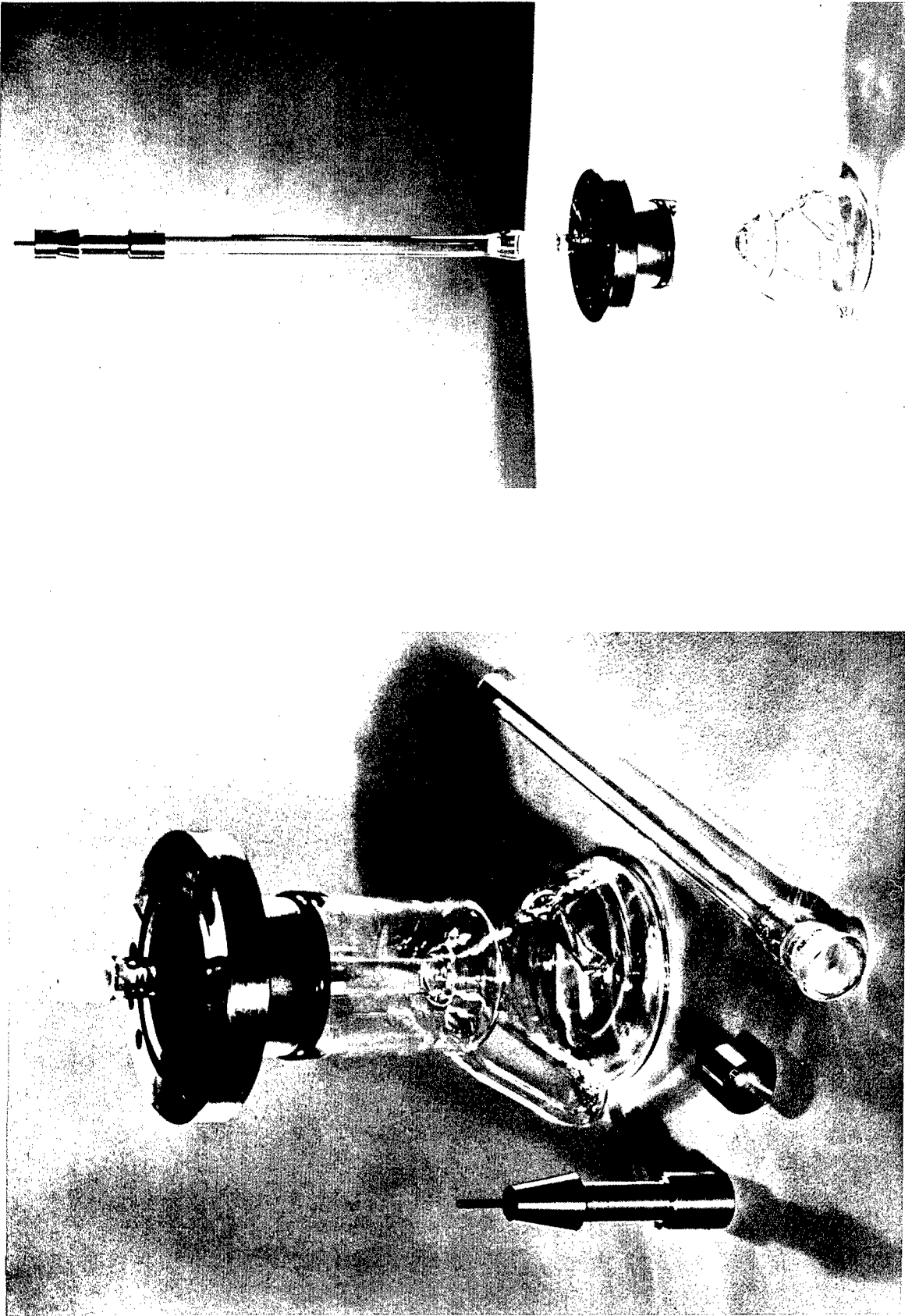
(a)

Fig. 5 - Demountable Boiler, Jet Stack, and Experimental Nozzle No. 1
(a) Disassembled   (b) Assembled

Liquid nitrogen traps used on the system are of two varieties (see Figs. 2 and 6). Type A traps are of standard spherical design with provision for cryogenic liquid in the inner sphere only. Liquid nitrogen is used following bake-out but only cold water is required during long runs. This procedure reduces the amount of mercury vapor that reaches the upper type B traps. Type B traps are of special construction with a double-wall outer dewar to provide cooling of both inner and outer spheres. Note that only one trap is used between the test chamber and B.A.G. 2 since large quantities of mercury are not transmitted to this trap due to the restricted conductance of the orifice (see Fig. 2). This latter trap is always activated with LN_2. The gauges are Varian-type UHV 12 Ionization gauges. Helium diffusers employed with the system are of two types. The pump speed measuring subsystem (see Fig. 3) uses a standard vycor tube with a throughput capacity of 0.1 micron liter/sec. The diffuser in the pressure differential measuring subsystem (see Fig. 4) employs a specially-constructed large-size quartz tube with an estimated throughput capacity of 1 micron liter/sec. This experimental diffuser will supply relatively large quantities of helium while maintaining impurity levels in the parts per million range.

An auxiliary pumping system which consists of a 5 liter/sec single stage mercury diffusion pump is used to provide a low forepressure for the main diffusion pump. It is also used to maintain a nonoxidizing vacuum (below 10^{-4} Torr) in the entire system when both the three-stage and experimental diffusion pumps are deactivated for bake-out. A Biondi-type chemical trap is inserted in the foreline. Activated alumina is used to reduce oil backstreaming from the mechanical pump. A mercury McLeod gauge is connected to the high vacuum side of the single stage pump to monitor operating forepressures of the main diffusion pump (while extracting the mercury partial pressure) and pressures during bake-out cycles. (The ionization gauges cannot be used during bake-out due to the high vapor pressure of mercury.)

Special furnaces, both fixed and movable, have been constructed to fulfill the bake-out requirements (200° to 350°C). The fixed type furnace uses the glass structure as a frame onto which the heater elements are mounted. The materials used for construction of the furnaces are: aluminum foil, asbestos, and fiberglass insulated heating tape. They are used in the following manner: A layer of foil is wrapped onto the glass to insure even heat distribution. The heater tape is then mounted preceded by a thin layer of asbestos to reduce the possibility of a short circuit through the aluminum foil. A thick layer of· asbestos is then applied to provide thermal insulation. Since the asbestos is applied when wet, it conforms easily to the contour of the apparatus to provide a compact and convenient bake-out arrangement.
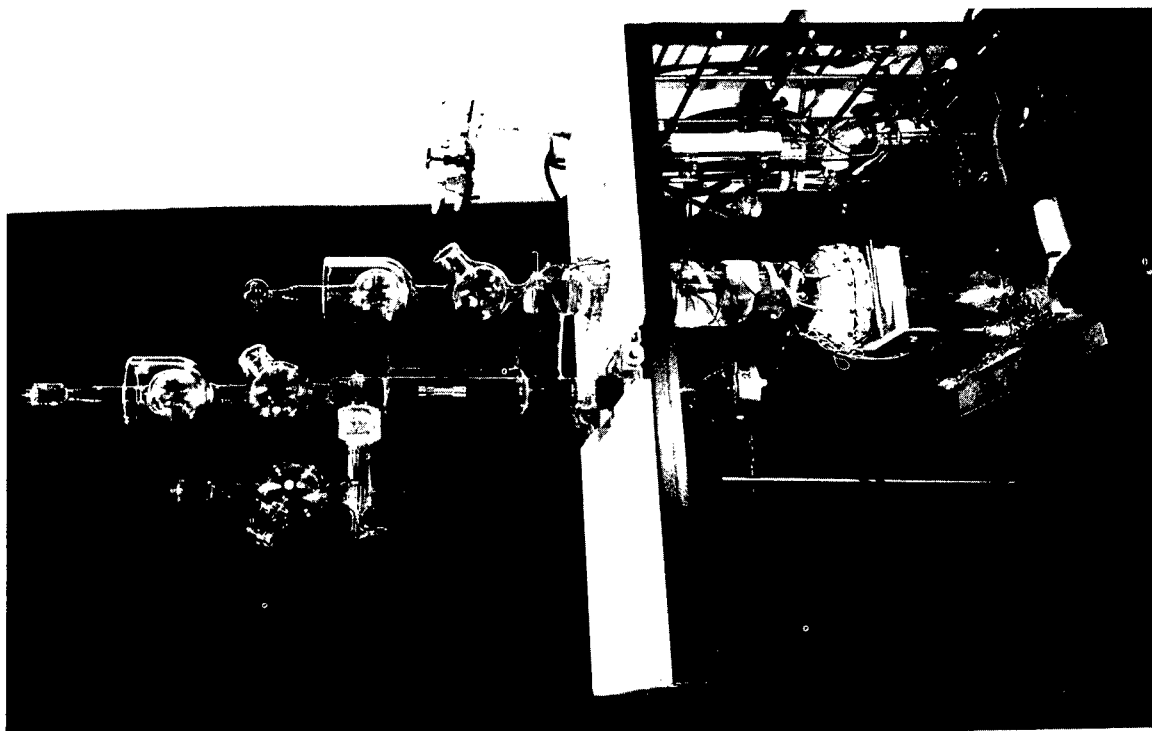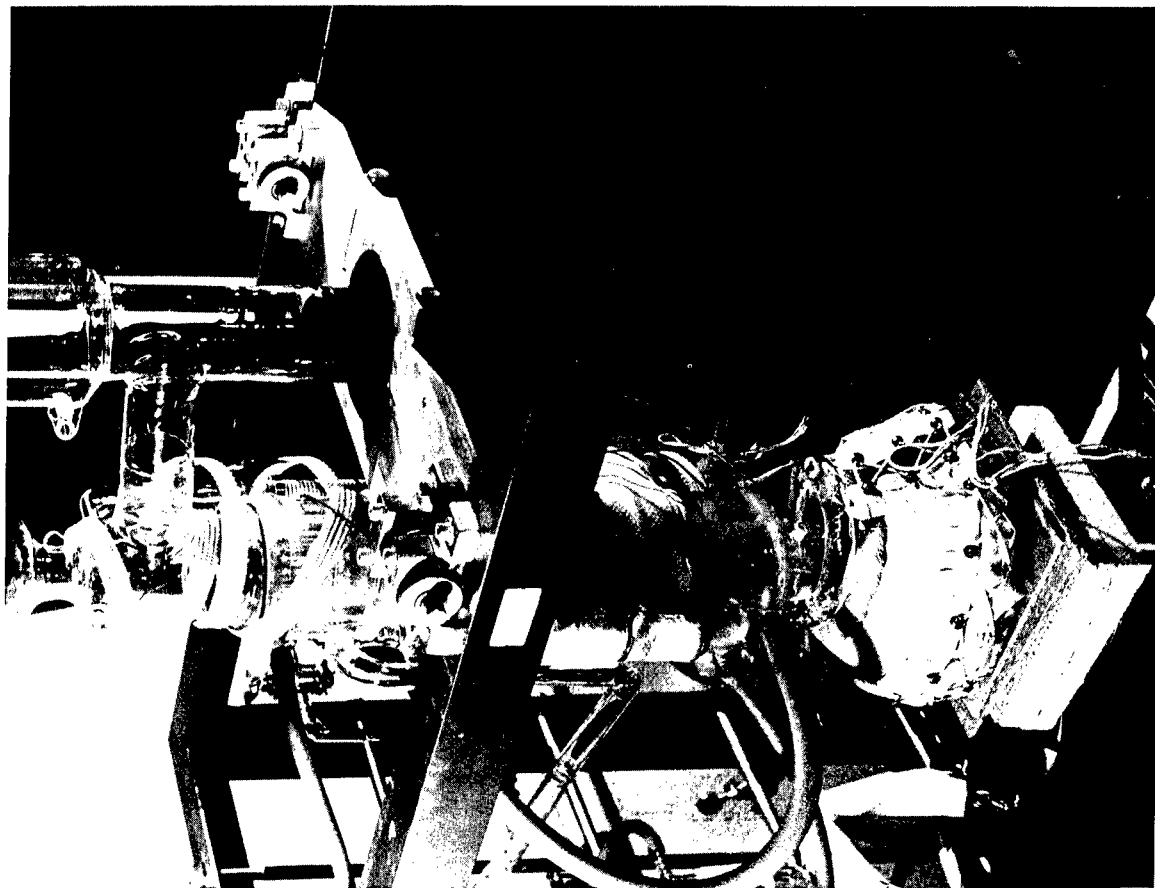
Fig. 7 – Three-Point Suspension Arrangement for Vapor-Jet Test System, i.e., Base of Diffusion Pump and Two-Pin Bearings

Fig. 6 – Vapor-Jet Test System

The movable furnaces, used for baking the gauges, are cylindrically shaped devices capped at one end and constructed similar to the fixed furnaces. These units are formed on molds which provide the proper dimensions to enclose the ion gauges. When the asbestos dries it becomes sufficiently rigid so that the heating elements require no additional support.

Because of the extended nature of the glass apparatus, the fixed furnace has been divided into six control zones. Each zone consists of heater tapes 2 ft. in length, wired in parallel, and controlled by a Variac. At least one iron-constantan thermocouple monitors the temperature of each zone. In addition, the movable furnaces have been divided into four control zones: (1) B.A.G. 1 and B.A.G. 3, (2) B.A.G. 2, (3) test chamber, and (4) the demountable boiler assembly. Each of these zones is also monitored by at least one iron-constantan thermocouple.

A three-point suspension system was constructed to hold the major glass apparatus (see Fig. 7). Two pivot bushings are mounted on a steel frame bench. The stainless steel flange at the lower end of the test chamber is attached to these pivot points. The base of the three-stage pump forms the third suspension point. The flanges can be bolted together without straining the glassware since the pivot assembly restricts two degrees of freedom.

Thermal expansion of the metal support arms, shown in Fig. 7, may cause a strain in the glassware during bake-out. Therefore coils of 1/8 in. copper tubing (not shown in Fig. 7) have been wound onto these arms adjacent to the stainless steel flange. A regulated flow of water through these coils maintains the temperature of the support arms at a safe level throughout the degassing cycle.

3. Performance tests with the experimental diffusion pump: Performance of the vapor-jet test system has been evaluated and found to be satisfactory. Photographs of the experimental vapor-jet at various boiler pressures have been taken. Pumping speed and pressure differential data have been collected and tabulated for various boiler pressures. Results indicate that high vacuum pump stages should be operated at low boiler pressures for greatest pump speed while backing stages should operate with high boiler temperatures to maintain large pressure differentials.

The design for the experimental nozzle used in the evaluation of this system is shown in Fig. 8. The gap dimension for these tests was set at 1.24 mm. (0.049 in.). The system was baked for 4 hr. at 200°C before activating the test nozzle. The boiler pressure was raised in stages and photographic studies (as described above) were conducted at various times. Figure 9 shows some typical photographs of the jet stream action at various boiler pressures.

7/8 DIA.

1/2 DIA

GAP ADJUSTED BY TURNING CAP

5-44NF-2B

EDGE TO BE SHARP

3/4

3/16

5/8

1/8R

.600 DIA

1 7/16

3 1/2

1/8R

1/8

1 1/16

3/4

1/2

REAM .499 DIA −.000
+.005

19/32 DIA.

7/8 DIA.
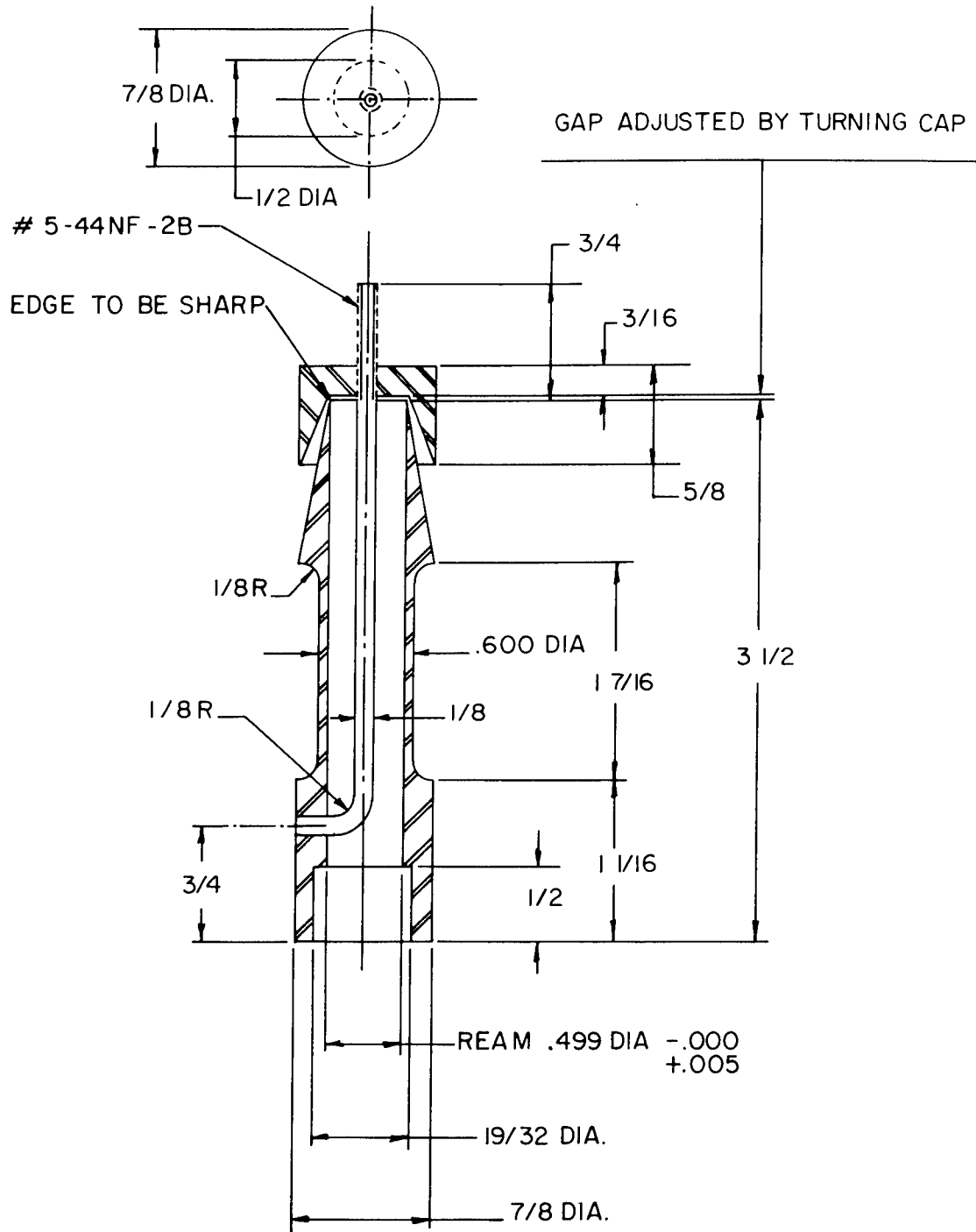
MAT'L - STAINLESS STEEL

Fig. 8 - Dimensional Drawing of Experimental Nozzle No. 1

- 16 -
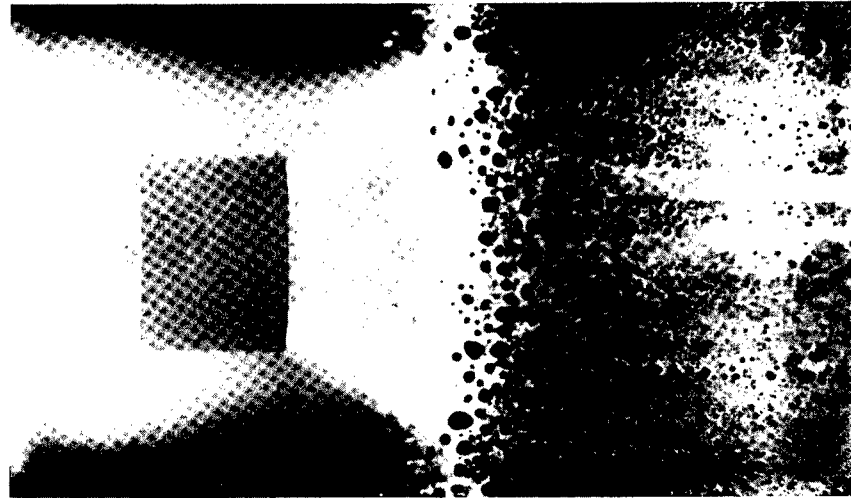
150°C   180°C   230°C

Fig. 9 - Photographs of a Glow Discharge in the Vapor-Jet Test Chamber at Various Boiler
Temperatures; Note the Different Expansion Angle of the Vapor-Jet

Pump speed and pressure differential measurements (as described on pages 6-9) were made and these results are shown in Fig. 10. The total pressure above the test chamber during these measurements was $\approx 10^{-7}$ Torr. The pump speed measurements show a peak operation for a boiler pressure which is lower than that required to maintain a large pressure differential. The pressure differential curve was not extended to maximum because the nozzle assembly was raised off the jet stack by the boiler pressure ($\cong 50$ Torr) at this point.

The above result suggests that it may be well to consider the use of two diffusion pumps or one pump equipped with two boilers so that the backing stages can be operated at a higher boiler pressure than the high vacuum pumping stage.
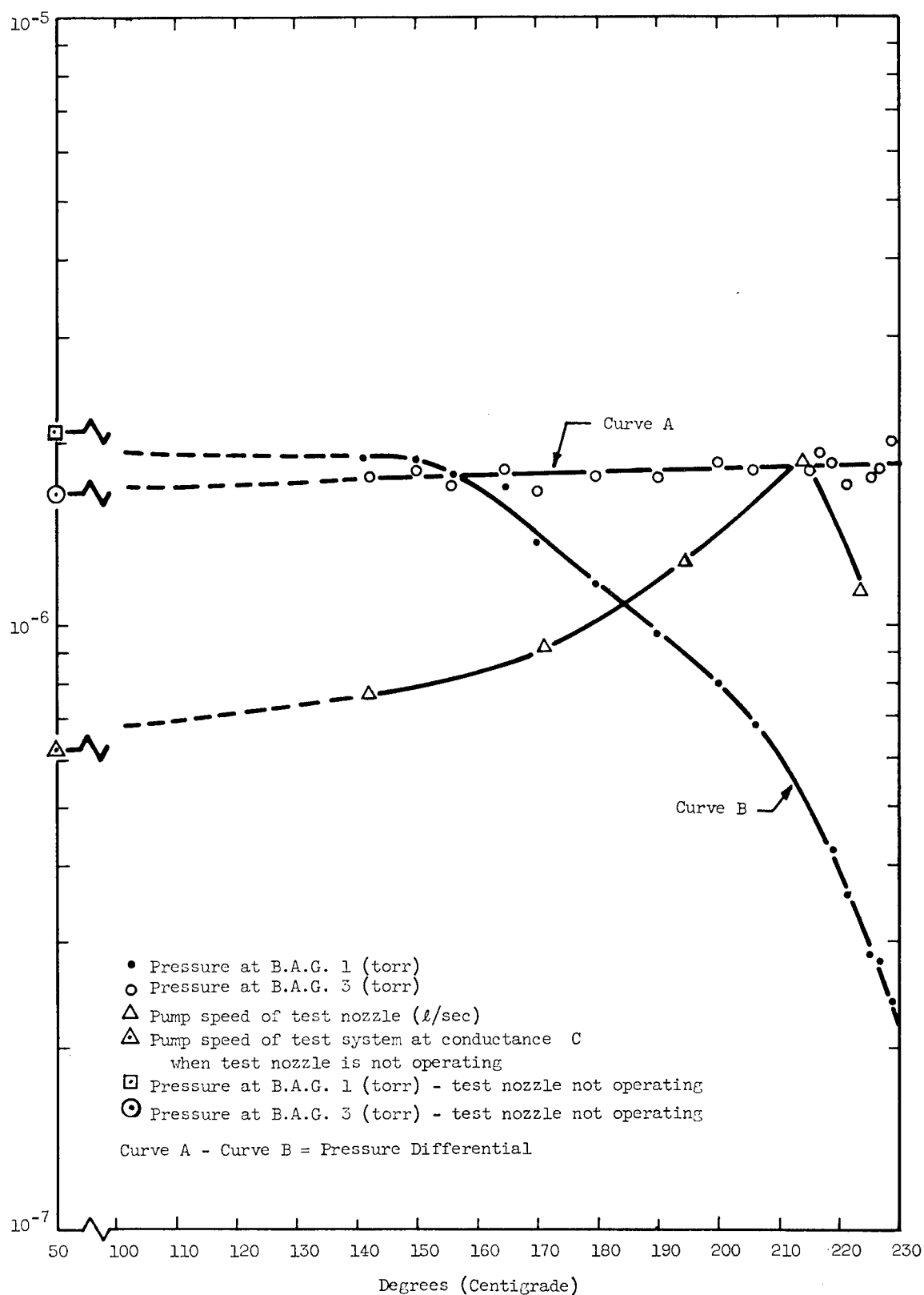
Fig. 10 - Plot of Pump Speed Data and Pressure Differential Values for an
Experimental Vapor-Jet vs. the Boiler Temperature

- 19 -

II. DETERMINATION OF THE QUANTITIES AND SPECIES OF GAS ABOVE GETTER-ION PUMPS AND CHEMICALLY TRAPPED OIL DIFFUSION PUMPS

An extremely sensitive gas analyzer has been used to study the operation of getter-ion pumps, diffusion pumps, and a special cryo-adsorbent trap.

A. Equipment and Techniques

A General Electric partial pressure analyzer, Model 514, tube type ZS 8008, has been obtained with several modifications. This instrument was originally described by Davis and Vanderslice.[10] The modifications have been described by Davis.[11] The analyzer tube uses a Nier-type, electron-bombardment ion source, a 90° sector magnetic analyzer with a 5 cm. radius of curvature, a 2.85 kilogauss permanent magnet, and a 10-stage electron-multiplier ion detector. The tube and magnet are bakeable to 425°C. The ion source contains a thoria-coated iridium filament which has a low work function and thus operates at a lower temperature than a tungsten filament. Both the disassociation of gases and the radiation heating of neighboring components in the ion source are greatly reduced. In addition, the source contains a second ionizing current filament of spiral tungsten design. Another special filament of spiral tungsten design has been placed in close proximity to the ion cage for degassing metal parts by electron bombardment. It is mounted laterally in the tube to prevent electron bombardment of the glass envelope (thus avoiding the erroneous production of gases by decomposition of glass).

Since it is desirable to mount the analyzer tube rigidly (for accurate alignment in the magnetic field), a bellows assembly was used to mechanically isolate the glass envelope from the vacuum plumbing. A special universal joint was built to withstand the 25 lb. of atmospheric compressive loading on the bellows when it is evacuated.

The getter-ion pumped vacuum system (Figs. 11, 12(a) and 12(b)) was equipped with several experimental parts. A Varian ionization gauge monitors total pressures in the system down to the 10^{-11} Torr range. An auxiliary vacuum system using diffusion pumps was also necessary because of the unsatisfactory operation of the getter-ion (8 liters/sec) pump when pumping relatively large amounts of helium. The auxiliary system has: a special cryo-adsorbent trap (Fig. 13), a UHV 2-in. diffusion pump with a water cooled chevron trap, a 1-in. booster diffusion pump, a valve, a bakeable foreline chemical trap, and a mechanical pump. All joints beyond the foreline of the booster pump are welded or sealed by metal gaskets (gold above 2-in. pump and above chevron trap, aluminum above booster pump, and copper elsewhere). The diffusion pumps were filled with DC-705 fluid.

TO TEST OR AUXILIARY EQUIPMENT

3

2

4

| ION PUMP | BAKEABLE VALVE | ION GAUGE | BELLOWS ASSEMBLY | PARTIAL PRESSURE ANALYZER TUBE |

BAKE ZONE

LN$_2$-ABSORBENT TRAP

COOLING WATER

WATER COOLED CHEVRON TRAP

⊗→ SUPPLY
→ EXHAUST

UHV DIFFUSION PUMP

⊗→ SUPPLY } FOR DIFFUSION
→ EXHAUST } PUMP WALLS

⊗→ SUPPLY } FOR BOILER
→ EXHAUST } COOLING COIL

BOOSTER DIFFUSION PUMP

⊗→ SUPPLY
→ EXHAUST

VALVE

FORELINE TRAP

MECHANICAL PUMP

AUXILIARY VACUUM SYSTEM

Fig. 11 - Schematic of Auxiliary Vacuum System and Partial Pressure Analyzer
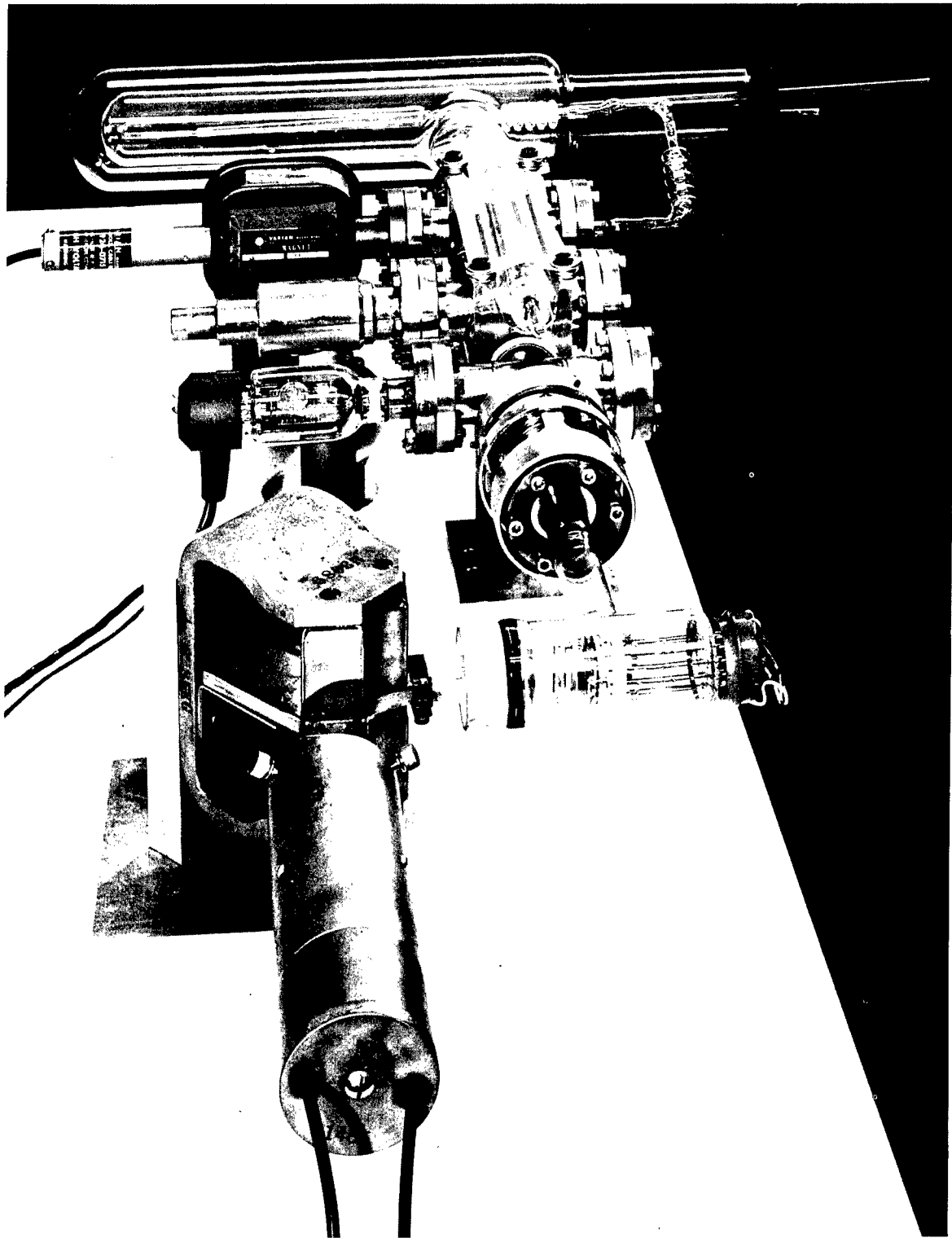
Fig. 12(a) - Partial Pressure Analyzation System
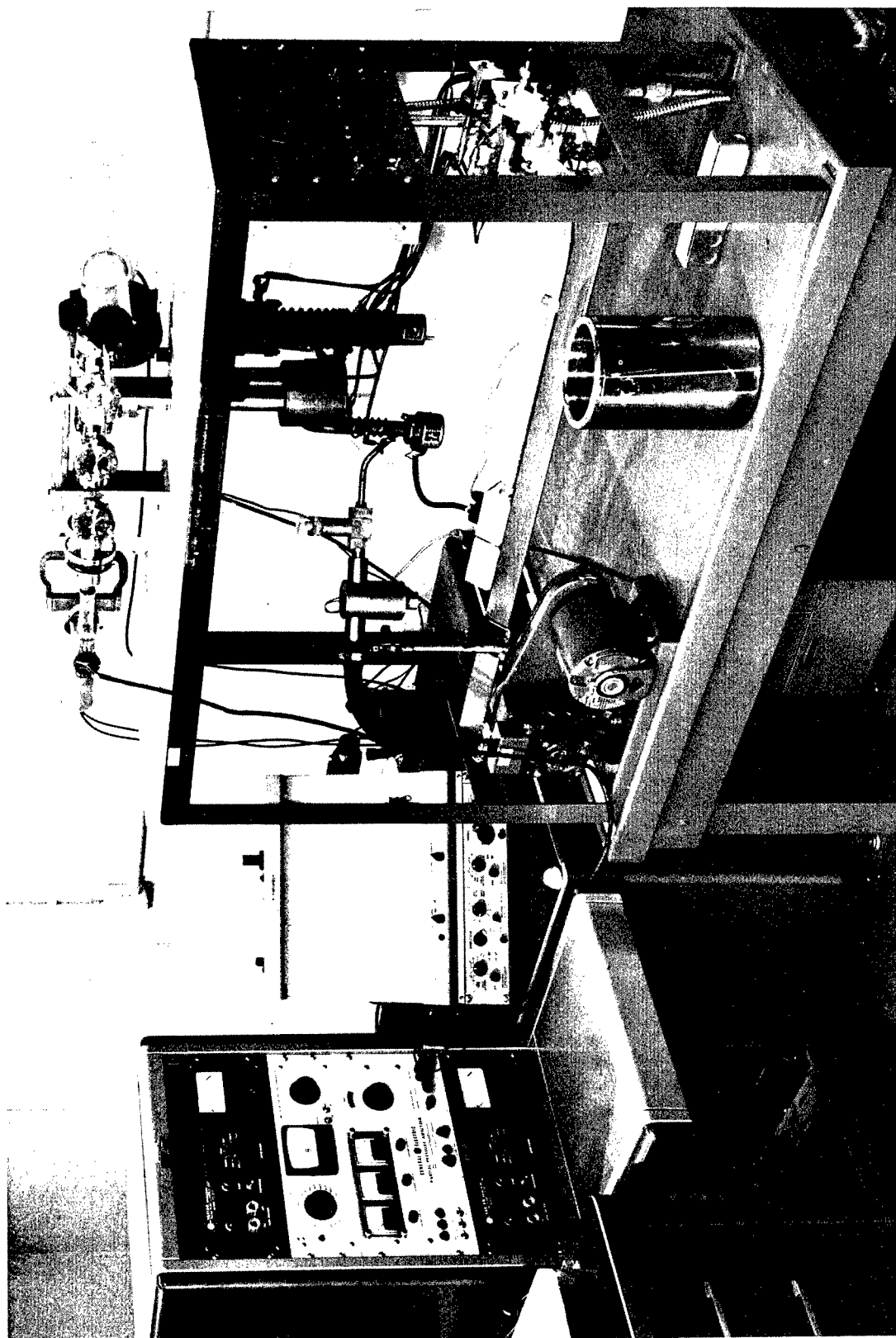
Fig. 12(b) - Partial Pressure Analyzation System and Auxiliary Vacuum System

1½" O.D.
NOMINAL
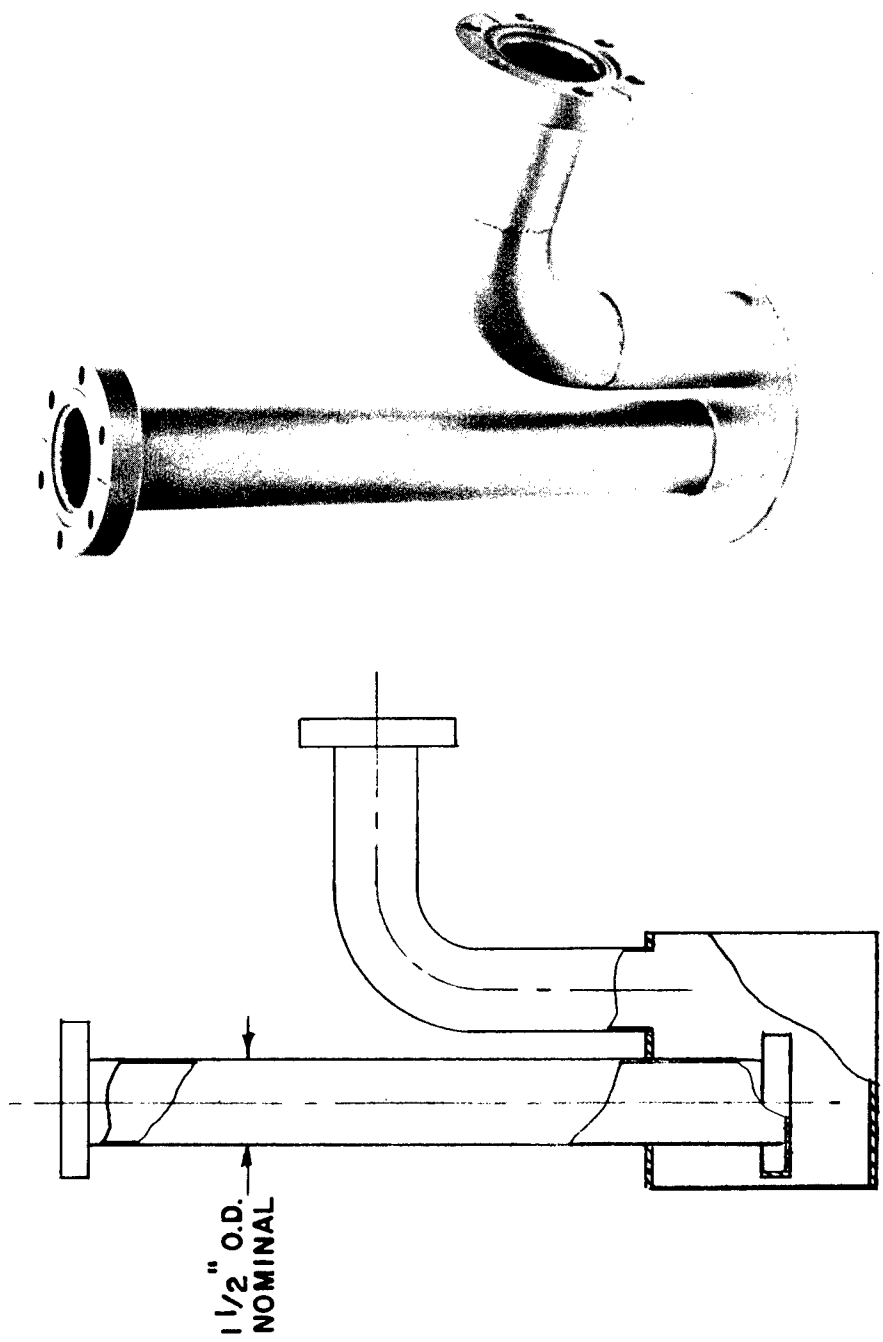
Fig. 13 - Special Liquid Nitrogen and Chemical Adsorbent Trap for Use Above an Oil Diffusion Pump (Auxiliary Vacuum System). A Partial Pressure Analysis Has Determined the Effect of Zeolite Trapping at 24°C and -195°C

The specially designed cryogenic and chemical adsorption trap shown in Fig. 13 is constructed of 304 stainless steel and is similar in design to the chemical trap proposed by Biondi.[12] Zeolite, activated alumina, or some other active adsorbent may be placed in the annular tray, at the bottom of the vertical tube, and in the bottom of the 4-1/2 in. O.D. chamber. (Zeolite was used for the present tests.) The trap is all heli-arc welded, and thus fully bakeable. In operation, a dewar filled with liquid nitrogen is raised around the entire trap.

The bake-out zone (including the auxiliary vacuum system) has been selected to enclose all degassing surfaces which are in proximity to the UHV region. The first diffusion pump jet can also be thoroughly outgassed (Fig. 11). All of the stainless steel tubing used above the bakeable valve (including the valve itself) has been electropolished. Also, prior to assembly, this equipment was chemically cleaned in an ultrasonic bath. These procedures have been employed to speed degassing and assure the lowest value of desorption. The auxiliary vacuum pumps permit: (1) thorough baking (including the getter-ion pump); (2) high pumping rates for inert gases; and thus (3) lower ultimate pressures during the course of special experiments.

B. Results

Figures 14 and 15 show the cracking patterns for the residual gases above a getter-ion pump and a chemically-trapped oil diffusion pump, respectively. The nonintegral peaks at m/e = 16.2, 17.2, 19.2, 35.6, and 37.6 are quite unexpected. These positions appear in both Figs. 14 and 15. The origin of the ions corresponding to these peaks is believed to be attributable to surface ionization stimulated by electron bombardment of metal cage parts.[13] The ions are then accelerated into the slit system at a preferred angle. This angle is such that the ions following this trajectory produce nonintegral peaks. Such peaks would only be detectable if a relatively large number of surface ions were produced at a localized region of the ion cage. If surface ions were produced in large numbers at all points of the cage, integral peaks would be randomly broadened so as to obscure the nonintegral ones.
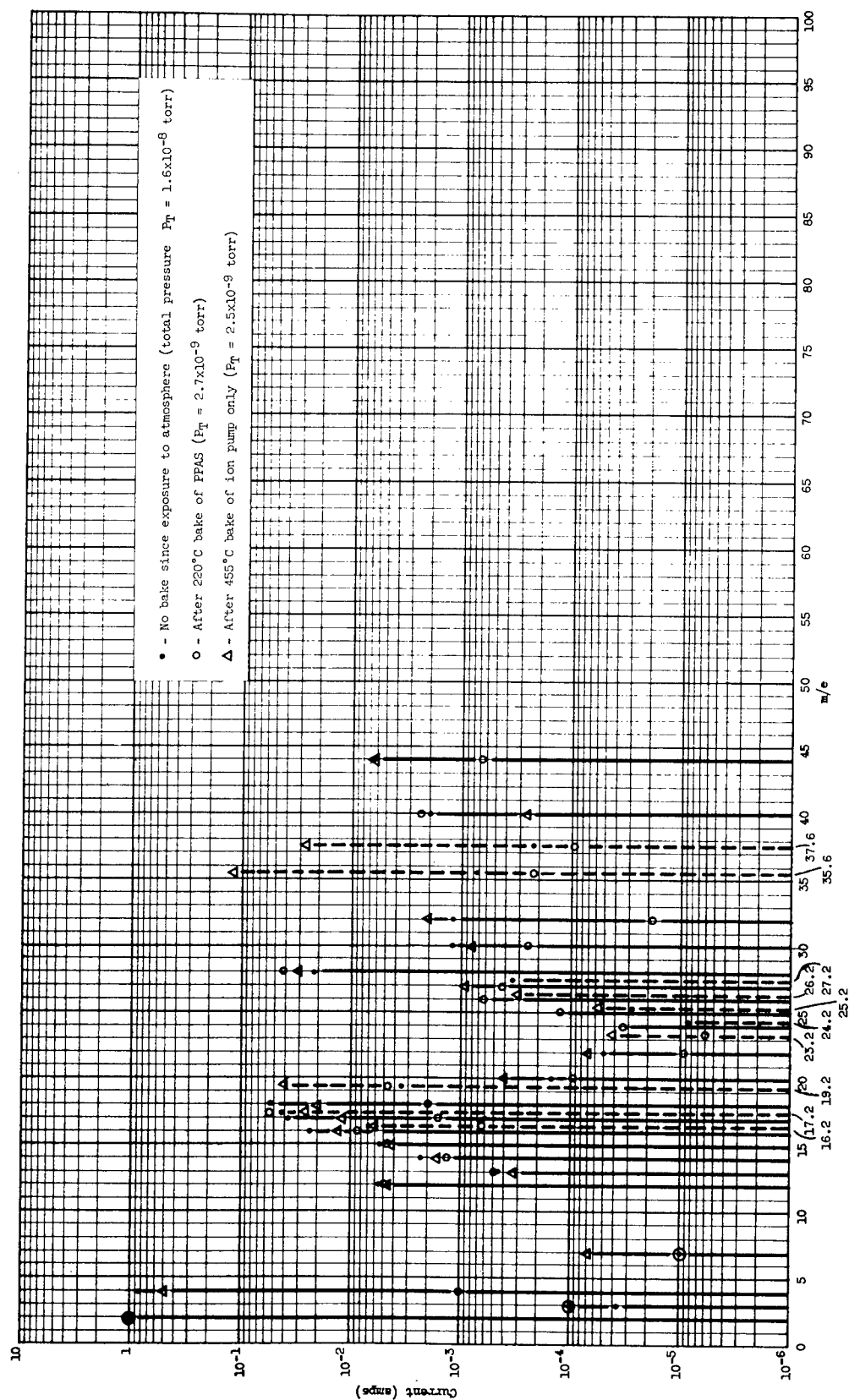
Fig. 14 - Bar Graph Showing Three Cracking Patterns (Normalized to H_2) of the Residual Gas Above a Getter-ion Pumped System After Various Treatments (See Legend). The Solid Bars Represent m/e = Integers Whereas the Broken Bars Represent m/e = Nonintegers.
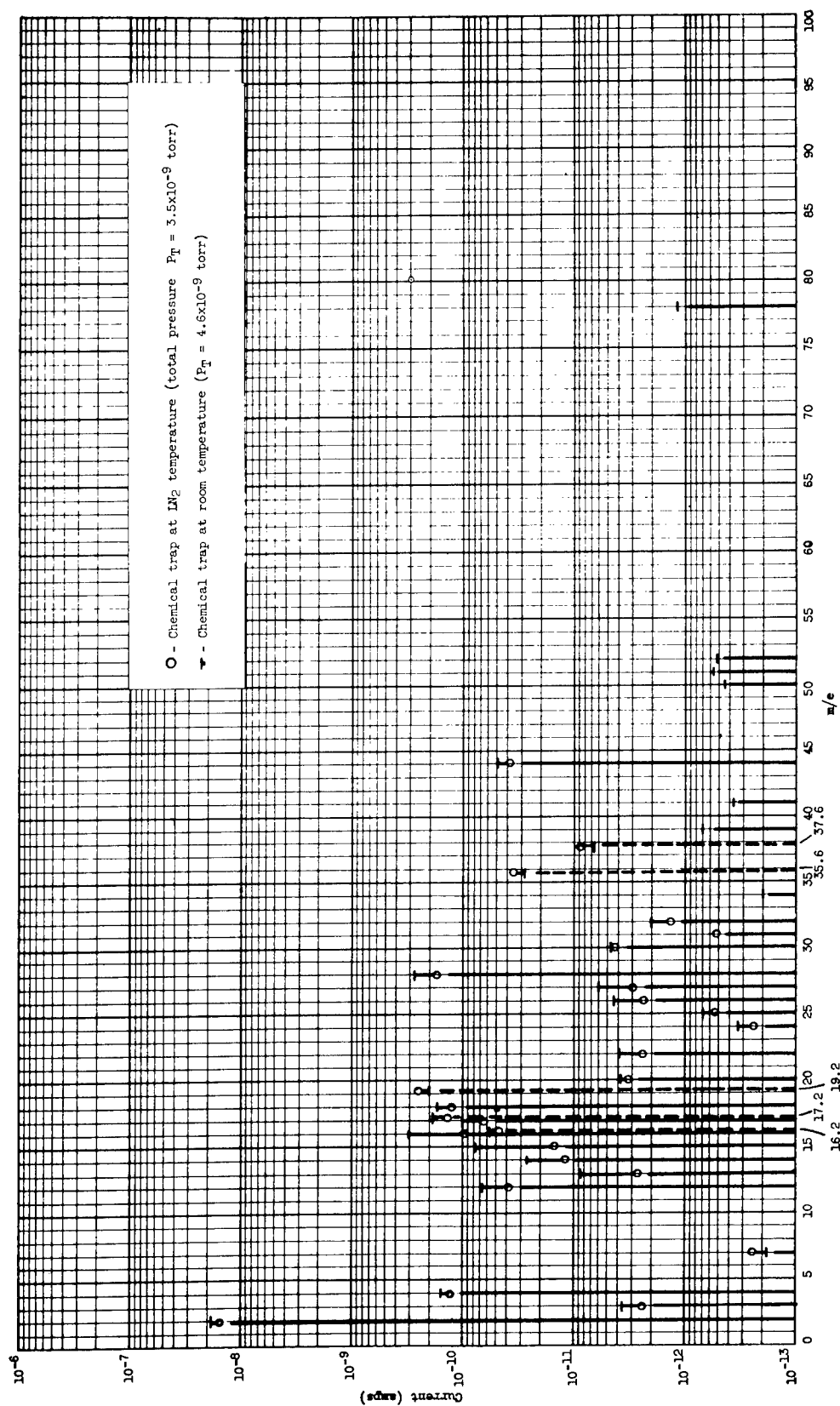
Fig. 15 - Bar Graph Showing the Cracking Pattern of the Residual Gas Above a Chemically-Trapped Oil Diffusion Pump. The Solid Bars Represent m/e = Integers Whereas the Broken Bars Represent m/e = Nonintegers.

Lichtman[13]/ has reported that nonintegral peaks are due to the following ions:

$$16.2* \quad 16+ \quad = O^+ \longleftarrow \text{adsorbed CO + electron bombardment.}$$

$$17.2 \quad 17+ \quad = OH^+ \longleftarrow \text{adsorbed } H_2O \text{ + electron bombardment.}$$

$$19.2 \quad 19+ \quad = F^+ \text{ (surface ion generated by electron bombardment of metal cage).}$$

$$\left.\begin{array}{ll} 35.6 & 35+ \\ 37.6 & 37+ \end{array}\right\} = Cl^+ \text{ (surface ion generated by electron bombardment of metal cage).}$$

Based on the above discussion it will be assumed (for the following analysis) that the ions represented by these nonintegral peaks exist in negligible amounts in the gas phase.

Figure 14 presents an analysis of the gases present in a getter-ion pumped vacuum system. The system used for these studies is shown in Fig. 12. Mass spectrums were obtained following three different treatments of the system: (I) a pump down to 1.6×10^{-8} Torr without a bake; (II) a bake of the entire system at 220°C (the electron multiplier was baked at 425°C to activate the dynodes with cesium); and (III) a bake of the ion-pump at 455°C, while the remainder of the system was at room temperature. The three sets of data were normalized with respect to H_2 and plotted together in Fig. 14. Mass spectra following conditions I, II, and III are identified by three symbols, respectively: . (dot); o (circle); and Δ (triangle).

The ratios between the H_2 sensitivities for each set of data were calculated and used to compile Table II.

---

* The numbers reported in this column are peculiar to our analyzer and do not necessarily correspond exactly with Lichtman's values.

TABLE II

COMPARISON OF RELATIVE CHANGES IN RESIDUAL GAS AS A FUNCTION OF CONDITIONS I, II, AND III

Condition:	I	II	III
Indicated Total Pressure:	1.5×10^{-8} Torr	2.7×10^{-9} Torr	2.5×10^{-9} Torr
Calculated Pressure of H_2:	1.4×10^{-8} Torr	4.3×10^{-9} Torr	2.5×10^{-9} Torr
Mass Two Peak Height:	9.5×10^{-9} Amp	1.6×10^{-7} Amp	3.5×10^{-9} Amp
Sensitivity for H_2:	1.5 Torr/amp	2.7×10^{-2} Torr/amp	7.1×10^{-1} Torr/amp
Normalized Sensitivities:	56	1	26
H_2	5.6×10^{1}	1.0	2.6×10^{1}
He	4.6×10^{1}	1.0×10^{-3}	1.3×10^{1}
Li	5.6×10^{-4}	1.0×10^{-5}	1.8×10^{-3}
H_2O	3.0	2.0×10^{-3}	5.5×10^{-1}
CH_4	3.3×10^{-1}	4.2×10^{-3}	1.1×10^{-1}
CO_2	3.5×10^{-1}	6.8×10^{-4}	1.7×10^{-1}
O_2	6.7×10^{-2}	1.9×10^{-5}	5.2×10^{-2}
A	1.1×10^{-1}	2.4×10^{-3}	7.3×10^{-3}
NO	6.7×10^{-2}	2.5×10^{-4}	2.1×10^{-2}
CO	1.2	4.3×10^{-2}	8.6×10^{-1}
C_2H_4	3.2×10^{-2}	7.1×10^{-4}	1.4×10^{-2}
O^+	3.8×10^{-1}	6.2×10^{-4}	1.6×10^{-1}
OH^+	2.4	5.6×10^{-2}	7.3×10^{-1}
F^+	2.0×10^{-1}	4.8×10^{-3}	1.18
Cl^+	4.2×10^{-2}	2.2×10^{-4}	3.1

Note: To obtain partial pressure analyzer output currents for the above gases, multiply values under:
Condition I by 1.70×10^{-10} amp
Condition II by 1.60×10^{-7} amp
Condition III by 1.35×10^{-10} amp

Most of the lines on the spectrum (Fig. 14) can be accounted for by the first 10 gases listed in Table II. However, the group of lines between m/e = 23.2 and 27.2 are not as easily identifiable. These are probably due to some hydrocarbon such as C_2H_4 which may have metastable ions in the 10^{-8} to 10^{-9} Torr pressure range. These metastable ions could account for the nonintegral peaks in this region of the spectrum.

A particularly large increase of (surface) F^+ and Cl^+ ions was noted following the 455°C bake of the ion pump. It is interesting to note that HCl and HF acids are used in the commercial cleaning process for these pumps. It is not unlikely that trace amounts of these agents remained in the pump after the cleaning procedure and were liberated by the high temperature (455°C) bake of the ion pump.

Figure 15 shows the mass spectrum above a chemically-trapped oil diffusion pump. The two sets of data points represent the operation of the chemical trap at room temperature (-) and at liquid nitrogen temperature (o).

The residual gases in the system during this study were CH_4, H_2O, He, H_2, Li, CO_2, CO, NO, and O_2. Also, there is a group of hydrocarbon peaks at m/e = 24, 25, 26, and 27. The amounts of these residual gases do not appear to be affected greatly by the chemical trap temperature. However, note the absence of peaks 78, 50, 51, 52 and 39 when the trap is at LN_2 temperature. These peaks coincide with the most intense parts of the benzene cracking pattern. The benzene pattern is characteristic of the DC-705 pumping fluid.[14] This result indicates that at room temperature a chemical trap is not sufficient for reducing backstreaming, if a vacuum system is to operate at a very low pressure (<10^{-11} Torr).

III. A PHYSICAL ADSORPTION ISOTHERM FOR INERT GASES

The conventional Brunauer-Emmett-Teller (BET)[15] adsorption isotherm is based on the physical adsorption of inert (negligible intermolecular interactions) gases by a solid. This isotherm, although based on a physically unrealistic model, met with such general success that a new calculation based on an improved model[16] (see Fig. 16, p.32) has been developed which retains much of the simplicity of the BET adsorption isotherm. To facilitate understanding, the model will be developed in two independent steps. In subsection A, the adsorption isotherm for a triangular site model is derived assuming the energies of adsorption to be known. In subsection B, equations for the energies of adsorption are derived. The isotherm equations are solved, and discussed in C. Subsection D contains numerical predictions for some useful adsorption systems.

A. Derivation of the Triangular Site Adsorption Isotherm

The derivation given here is based on the discipline of statistical mechanics. Let X_r be the number of adsorbed particles in the r-th layer. Then the total number of adsorbed particles, A , is given by $A = \sum_{r=1}^{M} X_r$, and $0 < X_M \leq X_{M-1} \leq \ldots \leq X_2 \leq X_1 \leq B$, where B is the total number of adsorption sites on the surface of the adsorbent and M is the number of layers containing adsorbed particles, i.e., $X_r = 0$ for all $r > M$. The number of ways in which A particles can be picked out of the total number of particles, N , leaving N_g particles in the parent gas is given by

$$\frac{N!}{N_g!A!} \tag{1}$$

where $N = N_g + A$. Of the A adsorbed particles, X_1 have to be assigned to the first layer, X_2 to the second layer, etc.; this can be done

$$\frac{A!}{X_1!X_2!\ldots X_M!} \tag{2}$$

different ways. The number of ways X_1 particles can be assigned to B sites is

$$\frac{B!}{(B-X_1)!}$$

and, in general, the number of ways X_r particles can be assigned to S_r sites on top of the X_{r-1} particles is given by

$$\frac{S_r!}{(S_r-X_r)!} \quad , \quad S_1 = B \quad . \tag{3}$$

Finally, the number of ways N_g particles can be assigned to the energy states in the parent gas with a specified distribution-in-energy $\{n_{gj}\}$ is the Boltzmann count:

$$N_g! \prod_j \frac{\omega^{n_{gj}}}{n_{gj}} \quad , \tag{4}$$

where n_{gj} is the number of gas particles in the j-th energy level of the gas and ω_{gj} is the degeneracy weight of the j-th energy level. The total number of ways, C , that N particles can be assigned to the over-all system is then given by the product of all the numbers in Eqs. (1-4), divided by $N!$ to account for the indistinguishability of the particles:

$$C = \frac{S_1!S_2!\ldots S_M! \prod_j \frac{\omega_{gj}^{n_{gj}}}{n_{gj}}}{X_1!X_2!\ldots X_M!(S_1-X_1)!(S_2-X_2)!\ldots(S_M-X_M)!} \quad . \tag{5}$$

In the BET theory the sites are given by

$$S_r = X_{r-1} \; , \; X_0 = B \quad ,$$

but this is physically unrealistic since it assumes that a particle is equally likely to be adsorbed at a point of neutral equilibrium (sitting on top of only one particle in the next lower layer) as to be adsorbed at a true equilibrium point. To avoid this difficulty assume that an adsorbed particle must be attached to three particles in the next lower layer (see Fig. 16). This
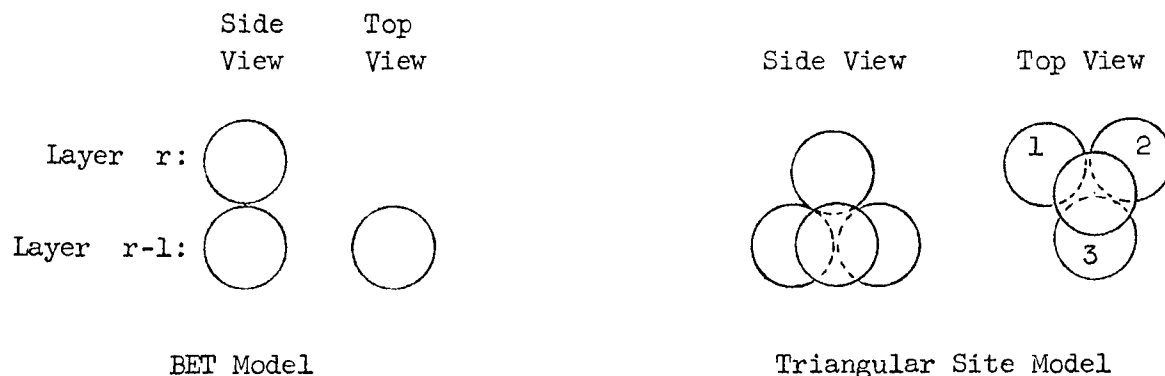
Fig.16 - Site Models

presumes the triangular site model to be one of true equilibrium, i.e., that intermolecular interactions do exist and are not negligible. We will require, however, that the intermolecular interactions be no stronger than the Lennard-Jones 4-5 potential. This is our definition of "physical adsorption". Further assuming that the particles are adsorbed randomly in location and are not mobile, i.e., lateral intermolecular interactions are neglected, the probability of site 1 (see Fig.16) being occupied is

$$\frac{X_{r-1}}{B} \quad ,$$

whereas the probabilities of sites 2 and 3 being occupied are, respectively, given by

$$\frac{X_{r-1}-1}{B} \quad , \quad \frac{X_{r-1}-2}{B} \quad .$$

Based on this model the number of sites, S_r , available for an adsorbed particle in the r-th layer is given by the product of the probability of three adjacent sites in the (r-1)-th layer being occupied simultaneously and the total number of possible sites, B:

$$S_r = X_{r-1}\left(\theta_{r-1} - \frac{1}{B}\right)\left(\theta_{r-1} - \frac{2}{B}\right) \quad ,$$

where $\theta_r = \dfrac{X_r}{B}$ is the decimal percentage occupancy of the r-th layer. Normally B is very large (on the order of 10^{15}) and hence S_r can be simply expressed as

$$S_r = X_{r-1}\theta_{r-1}^2 \tag{6}$$

to an excellent approximation. However, now S_r need not be an integer and the factorials in Eq. (5) are not defined. To circumvent this difficulty, the generalized factorial, the gamma function, will be used. Letting

$$X_0 = B \ , \ S_1 = B \ , \ \theta_0 = 1$$

Eq. (5) becomes

$$C = \dfrac{\displaystyle\prod_{r=1}^{M} \Gamma(X_{r-1}\theta_{r-1}^2+1) \prod_{j} \dfrac{\omega_{gj}^{n_{gj}}}{n_{gj}}}{\displaystyle\prod_{r=1}^{M} \Gamma(X_r+1) \prod_{r=1}^{M} \Gamma(X_{r-1}\theta_{r-1}^2-X_r+1)} \tag{7}$$

The statistical problem is to find the numbers X_r and n_{gj} that give a maximum value to $\ln C$, under the restrictions implied by a given total number of particles, N, and a given total energy, E, of the system. In other words, the entropy of the system is maximized. The restrictions on the system are given by

$$N = N_g + A = \sum_{j=1}^{\infty} n_{gj} + \sum_{r=1}^{M} X_r \quad , $$

$$\tag{8}$$

$$E = \sum_{j=1}^{\infty} n_{gj}\epsilon_{gj} - \sum_{r=1}^{M} X_r W_r \quad , $$

where ϵ_{gj} is the energy of the j-th energy level in the gas and W_r is the energy of adsorption for each adsorbed particle in the r-th layer. It is

commonplace to set all W_r , for $r > 1$, equal to the energy of evaporation from the liquid phase. However, the energies of adsorption will be investigated in the next section and for the present we simply assume them to be known quantities. Since N and E are constant and $\ln C$ is a maximum, their variations must vanish:

$$d(\ln C) = \sum_{r=1}^{M} dX_r \frac{d(\ln C_a)}{dX_r} + \sum_{j=1}^{\infty} dn_{gj} \frac{d(\ln C_g)}{dn_{gj}} = 0 \quad ,$$

$$dN = \sum_{r=1}^{M} dX_r + \sum_{j=1}^{\infty} dn_{gj} = 0 \quad , \tag{9}$$

$$dE = \sum_{j=1}^{\infty} \epsilon_{gj} dn_{gj} - \sum_{r=1}^{M} W_r dX_r = 0 \quad ,$$

where $C = C_a C_g$, C_a being that part of the product pertaining only to the adsorbed particles and C_g that part pertaining only to the gas particles. Using the Lagrangian multipliers α , β , the following equation is obtained:

$$\sum_{r=1}^{M} \left(\frac{d \ln C_a}{dX_r} - \alpha + \beta W_r \right) dX_r + \sum_{j=1}^{\infty} \left(\frac{d \ln C_g}{dn_{gj}} - \alpha - \beta \epsilon_{gj} \right) dn_{gj} = 0 \quad .$$

In this expression independent variations of dX_r and dn_{gj} can be made. Consequently, the equation can only be satisfied if each expression enclosed by parenthesis is equal to zero, i.e.,

$$\frac{d}{dX_r} \ln C_a = \alpha - \beta W_r \quad , \tag{10}$$

$$\frac{d}{dn_{gj}} \ln C_g = \alpha + \beta \epsilon_{gj} \quad . \tag{11}$$

Equation (11) is the classical equation of an ideal gas treated separately from the adsorbed layers and, assuming n_{gj} very large, leads to the identification of α and β in terms of the chemical potential, μ , and the absolute temperature, T , of the gas phase:[17]

$$\alpha = -\frac{\mu}{kT} , \quad \beta = \frac{1}{kT} , \tag{12}$$

where k is the Boltzmann's constant. The ideal gas equation also follows:

$$pV = N_g kT \tag{13}$$

$$N_g = V \left(\frac{2\pi mkT}{h^2} \right)^{3/2} e^{\frac{\mu}{kT}} \tag{14}$$

where V is the volume, p is the pressure, m is the mass of a gas particle, and h is Planck's constant. These results are derived from the classical distribution-in-energy which is valid when[17]

$$\ln \left[\frac{V}{N_g} \left(\frac{2\pi mkT}{h^2} \right)^{3/2} \right] > 3 \tag{15}$$

If this validity equation is not satisfied, Bose-Einstein or Fermi-Dirac statistics must be used.

It is now convenient to define a new parameter, γ_r , such that

$$\gamma_r = e^{-\frac{\mu + W_r}{kT}} , \tag{16}$$

and to evaluate this new parameter in terms of physically measurable parameters. From Eqs. (13) and (14) we obtain

$$\gamma_r = \left(\frac{2\pi m}{h^2} \right)^{3/2} \frac{(kT)^{5/2}}{p} e^{-\frac{W_r}{kT}} . \tag{17}$$

Equation (10) can now be written as

$$\frac{d \ln C_a}{d\theta_r} = B \ln \gamma_r . \tag{18}$$

This is the basic equation to solve in deriving the adsorption isotherm. Differentiating Eq. (7) we obtain

$$\frac{d}{d\theta_r} \ln C_a = \frac{d}{d\theta_r} \left[\ln \Gamma(B\theta_r^3+1) - \ln \Gamma(B\theta_r+1) - \ln \Gamma(B\theta_{r-1}^3 - B\theta_r+1) \right.$$

$$\left. - \ln \Gamma(B\theta_r^3 - B\theta_{r+1}+1) \right] . \qquad (19)$$

All arguments of the gamma functions are certainly very, very large with the only two exceptions occurring at $r = 1$ and $r = M$. At $r = M$, $B\theta_M$ may be small, and at $r = 1$, $B\theta_1$ or $B(1-\theta_1)$ may be small. Since it is convenient to use the Stirling's approximation for the gamma functions of large arguments, these two cases will be excluded by requiring that $X_M \gg 1$, $B \gg X_1$, i.e., the following equations will not be valid for, say, the first 100 atoms to be added to the top layer and the last 100 atoms to be added to the bottom layer. However, we are nominally concerned with orders of magnitude of 10^{15} and, hence, these restrictions are relatively minor. Using Stirling's approximation in Eq. (19) we obtain

$$\frac{d}{d\theta_r} \ln C_a = B \left[3\theta_r^2 \ln \frac{\theta_r^3}{\theta_r^3 - \theta_{r+1}} + \ln\left(\frac{\theta_{r-1}^3}{\theta_r} - 1 \right) \right] , \qquad (20)$$

and

$$\gamma_r = \left(\frac{\theta_{r-1}^3 - \theta_r}{\theta_r} \right) \left(\frac{\theta_r^3}{\theta_r^3 - \theta_{r+1}} \right)^{3\theta_r^2} . \qquad (21)$$

The last equation, together with Eq. (17), completely defines the triangular site physical adsorption isotherm.

B. Derivation of the Energies of Adsorption

The energy of adsorption, W_r, is defined as the difference between the energy of a free particle at rest and the energy of an adsorbed particle in the r-th layer. We assume here that the energy of adsorption, W_r, of the r-th layer is the same value throughout the layer and is always positive. As

stated in the last section, it is commonplace to set all W_r , for $r > 1$ equal to the energy of evaporation from the liquid phase, W_ℓ , and to set W_1 equal to an experimentally determined energy of adsorption at low coverages. However, this cannot be justified since W_1 is usually at least a hundred times greater than W_ℓ and, hence, this assumption literally prevents any adsorbed particles from entering the second layer. The assumption is particularly bad when one notices that, from Eq. (17), the occupancy of upper layers is exponentially dependent on the energy of adsorption, i.e., a small difference in the energy of adsorption makes a large difference in the coverage. This subsection gives a detailed alternative based on a systematic evaluation of the intermolecular potentials.

Assume that the intermolecular potential between the adsorbed molecules, φ , can be closely approximated by the Lennard-Jones (n-m) potential:

$$\varphi(\rho) = 4\epsilon \left[\left(\frac{\sigma}{\rho}\right)^m - \left(\frac{\sigma}{\rho}\right)^n \right], \quad m > n ,^* \tag{22}$$

where ρ is the distance between the molecules, σ is the distance of closest approach of two molecules which collide with zero initial relative kinetic energy, and ϵ is the maximum energy of attraction of the two molecules.[18] The Lennard-Jones (6-12) potential is shown in Fig. 17. When the force constants, σ and ϵ , are unknown, they can be estimated in many ways, e.g., from the boiling point, melting point, Boyle temperature, second virial coefficient, etc.[18] Letting R be the equilibrium distance between the adsorbed molecules, it is necessary that

$$\left. \frac{d\varphi(\rho)}{d\rho} \right|_{\rho=R} = 0$$

i.e.,

$$R = \left(\frac{m}{n}\right)^{\frac{1}{m-n}} \sigma \quad . \tag{23}$$

---

* The exponent m should not be confused with the mass m . A double meaning is tolerated here since the context always unambiguously clarifies which meaning is to be used.
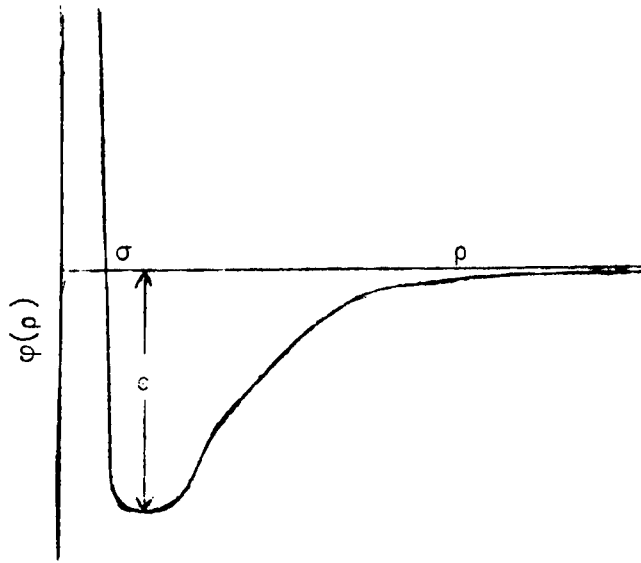
Fig. 17 - Lennard-Jones Intermolecular Potential

Similarly, the intermolecular potential between the adsorbed molecule and an adsorbent molecule, φ_I , can be approximated as

$$\varphi_I = 4\epsilon_I \left[\left(\frac{\sigma_I}{\rho}\right)^k - \left(\frac{\sigma_I}{\rho}\right)^\ell \right] \, , \, k > \ell \, . \tag{24}$$

When the interaction force constants, σ_I , ϵ_I , between the surface and adsorbed molecules are unknown, they can be estimated from the empirical rules of combination:

$$\epsilon_I = \sqrt{\epsilon \, \epsilon_s}$$

$$\sigma_I = \frac{\sigma + \sigma_s}{2} \tag{25}$$

where the force constants with the s subscript pertain to the surface molecules and those without subscripts pertain to the adsorbed molecules.

The term "physical adsorption" can now be explicitly defined as that adsorption for which

$$k > \ell > 3 \quad , \quad m > n > 3 \quad .$$

In other words, attractive forces arising from charges and permanent dipoles are excluded from consideration.*

Using the above intermolecular potentials, the part, W_s , of the W_1 energy of adsorption due to the solid adsorbent is given by

$$W_s = - N_o \iiint_V \varphi_I(\rho)dV \qquad (26)$$

where V denotes the entire volume of the solid adsorbent and N_o is the density per $\mathring{A}^3$ of the adsorbent molecules. The integration in Eq. (26) is an approximation to the actual atom-by-atom summation needed to evaluate W_s and implies that the intermolecular potentials are additive. This latter assumption is probably more serious than any made thus far but is necessary for any simple and usable theory.

Considering the surface to be an infinite plane located a distance D below the centers of the adsorbed molecules in the first layer (see Fig. 18, p.41), the integrations in Eq. (26) can be performed with the result that

$$W_s = 8\pi N_o \epsilon_I \left[\frac{\sigma_I^\ell}{(\ell-2)(\ell-3)D^{\ell-3}} - \frac{\sigma_I^k}{(k-2)(k-3)D^{k-3}} \right] \qquad . \qquad (27)$$

---

* Actually, the development presented here is valid for all $n > 2$ and the case $\ell = 3$ can be included in this theory by a simple extension. However, at this time the extra effort involved does not appear to be justifiable.

The maximum value of W_s will, of course, occur at the equilibrium value of D, i.e.,

$$\frac{dW_s}{dD} = 0 \quad .$$

Therefore,

$$D = \left(\frac{\ell-2}{k-2}\right)^{\frac{1}{k-\ell}} \sigma_I \quad . \tag{28}$$

Defining a new constant $C_{k\ell}$ such that

$$C_{k\ell} = \left(\frac{k-2}{\ell-2}\right)^{\frac{\ell}{k-\ell}} \frac{k-\ell}{(\ell-2)(\ell-3)(k-3)} \quad , \tag{29}$$

Eq. (27) can be simply written as

$$W_s = 8\pi C_{k\ell} N_0 D^3 \epsilon_I \quad . \tag{30}$$

Consider now the energy of adsorption for a molecule adsorbed in the first layer. This molecule interacts with the entire solid adsorbent, all of the other molecules adsorbed in the first layer, the molecules adsorbed in the second layer, and all remaining adsorbed molecules. Labeling the energy contributions from these interactions by W_s, W_{11}, W_{12}, and $W_{1j}(3 \leq j \leq M)$, respectively, we can write W_1 as

$$W_1 = W_s + W_{11} + W_{12} + \sum_{j=3}^{M} W_{1j} \quad . \tag{31}$$

The average value of the W_{11} term is approximately given by summing over the six nearest neighbors and integrating over the remaining plane of the first layer. The latter integration is performed from an arbitrary distance w from the center of the adsorbed molecule under consideration (see Fig. 18). However, since only θ_1 of the first layer is occupied, this factor must appear in the summation and integration. Letting

$$z(w) = 8\pi\epsilon\sigma_o w^2 \left[\frac{1}{n-2}\left(\frac{\sigma}{w}\right)^n - \frac{1}{m-2}\left(\frac{\sigma}{w}\right)^m \right] \quad , \tag{32}$$

where σ_o is the number of adsorbed molecules per $\overset{\circ}{A}^2$ in the first complete monolayer and is given by

$$\sigma_o = 1.1547 \ R^{-2} \quad ; \tag{33}$$

the W_{11} term can be written as

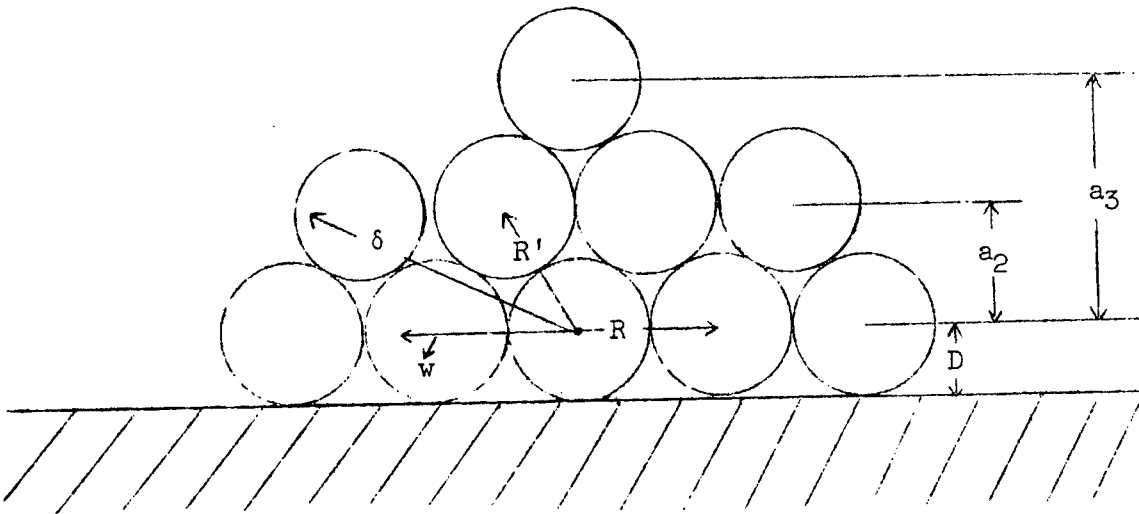$$W_{11} = \theta_1 \left[z(w) - 6\varphi(R) \right] \quad .^* \tag{34}$$

Fig. 18 - Adsorption Geometry

The W_{12} term is evaluated in a similar manner by summing over nearest neighbors and integrating over the remainder of the second layer. The result is

---

* The negative sign appears because $\varphi(R)$ is negative.

$$W_{12} = \theta_2 \left[z(\delta) - 3\varphi(R') \right] , \qquad (35)$$

where R' is the distance between the centers of the nearest neighbors in the second layer and the adsorbed molecule in the first layer, and δ is a new arbitrary parameter which is the smallest value of ρ used in the integration. The physical interpretation of R' and δ is shown schematically in Fig. 18.

The evaluation of W_{13} forces us to choose one of three routes. The third layer may be laid down in two possible ways. If the molecules in the third layer lie above the molecules in the first layer, the crystalline structure called hexagonal close-packed (hcp) results. Otherwise, the face-centered cubic (fcc) crystalline structure is obtained. It is a well known fact of solid state physics that there is virtually no difference in energies between these two crystalline structures. Therefore, we choose the third route - that of ignoring the crystalline structure by representing the third layer as an infinite plane and integrating over it. In performing the integration, however, the distance between the first and third layers must be known. As shown in Fig. 18, this distance is denoted by a_3 and, in general, the distance between the j-th layer and the first layer is denoted by a_j . These distances are easily evaluated by assuming all adjacent layers to be the same distance, a , from each other. Hence,

$$a_j = (j-1)a , \qquad (36)$$

and

$$W_{13} = \theta_3 z(a_3) . \qquad (37)$$

The remaining M-3 interaction energies are handled in the same manner.

Collecting the above results together, the energy of adsorption for a molecule in the first layer is given by

$$W_1 = W_s + \theta_1 \left[z(w) - 6\varphi(R) \right] + \theta_2 \left[z(\delta) - 3\varphi(R') \right] + \sum_{j=3}^{M} \theta_j z(a_j) . \qquad (38)$$

The evaluation of the energy of adsorption for a molecule in the r-th layer can now be determined. The energy of interaction with the surface, W_{rs}, can be calculated exactly as W_s was calculated by replacing D by $D+a_r$. The result is

$$W_{rs} = \frac{W_s}{k-\ell} \left[\frac{k-3}{(1+d_r)^{\ell-3}} - \frac{\ell-3}{(1+d_r)^{k-3}} \right],$$ (39)

where

$$d_r = \frac{a_r}{D} .$$ (40)

Treating the layers below the r-th layer exactly as the layers above the first layer were treated, and letting

$$\delta(r > 1) = 0 \quad \text{when} \quad r = 1 \quad,$$

$$= 1 \quad \text{for all} \quad r > 1 \quad,$$ (41)

the energy of adsorption for the r-th layer can be written as

$$W_r = W_{rs} - 3\left(\delta(r > 1) + \theta_{r+1}\right)\varphi(R') + \theta_r\left[z(w)-6\varphi(R)\right] +$$

$$+ (\theta_{r-1}+\theta_{r+1})z(\delta) + \sum_{j=1}^{r-2} \theta_j z(a_r-a_j) + \sum_{j=r+2}^{M} \theta_j z(a_j-a_r) \quad .$$ (42)

where $\theta_j = 0$ for all $j < 1$ and all $j > M$. Notice that, for $r > 1$, the second term does not contain θ_{r-1} but a 1 instead. This reflects the fact that, in the triangular site model, each adsorbed molecule must have three molecules immediately below it.

With tongue in cheek one can now be so bold as to ask what happens as r approaches infinity? The energy of adsorption as given by Eq. (42) should approach a value fairly close to the energy of evaporation, W_ℓ, of the adsorbate from its liquid state, i.e., $W_\infty \approx W_\ell$. Assuming that evaporation takes place from the top layer and that

$$\theta_{r-1} = \theta_r \simeq 0 \ , \ \theta_j = 1 \ \text{ for all } \ j \leq r-2 \ ,$$

the first and last term of Eq. (42) of course vanish and the next to last term becomes a difference, ψ , of two simple power series with definite, and well tabulated, limits. Thus

$$W_\ell = -3\varphi(R') + \psi \quad . \tag{43}$$

Due caution must be exercised, however, when this equation is used since the model on which it is based must break down as r becomes very large.

Although the values of w and δ are arbitrary, it is nonetheless desirable to ascertain their values in a systematic manner. The most logical method of determining the value of w is to require the integration result (for $\theta_r = 1$) at w to equal the correct result obtained by actually summing over the six next nearest neighbors lying within the r-th layer and lying at a distance of $\sqrt{3} \, R$ from the adsorbed molecule under consideration,[19] i.e.,

$$z(w) = -6\varphi(\sqrt{3}R) \quad . \tag{44}$$

For most cases of interest the terms which are a function of m are much smaller than the terms which depend on n and, hence, can be dropped with little error. With this approximation w can be determined as

$$w = \left[\frac{\pi\sigma_o R^2}{n-2} \right]^{\frac{1}{n-2}} \sqrt{3} \, R \quad . \tag{45}$$

Using a comparable argument for δ , we obtain

$$\delta = \left[\frac{2\pi\sigma_o(4R^2+3a^2)}{9(n-2)} \right]^{\frac{1}{n-2}} \sqrt{\frac{4}{3} R^2+a^2} \quad . \tag{46}$$

These equations conclude the evaluation of the energy of adsorption. However, Eq. (42) is clearly a function of X_r and we must therefore re-examine the derivation of the adsorption isotherm of the last section in

more detail. In fact, the differentiation of the last expression of Eq. (8) does not give Eq. (9) but, on the contrary, gives

$$dE = \sum_{j=1}^{\infty} n_{gj} d\epsilon_{gj} - \sum_{r=1}^{M} W_r dX_r - \sum_{r=1}^{M} \theta_r \sum_{j=1}^{M} \frac{dW_r}{d\theta_j} dX_j \quad . \tag{47}$$

The last term can be rearranged to yield

$$\sum_{j=1}^{M} \left(\sum_{r=1}^{M} \theta_r \frac{dW_r}{d\theta_j} \right) dX_j \quad , \tag{48}$$

and the term in parenthesis can be evaluated as

$$\sum_{r=1}^{M} \theta_r \frac{dW_r}{d\theta_j} = W_j - W_{js} + 3 \left(\delta(j > 1) + \theta_{j+1} - \theta_{j-1} \right) \varphi(R') \quad . \tag{49}$$

Thus Eq. (9) becomes

$$dE = \sum_{j=1}^{\infty} n_{gj} d\epsilon_{gj} - \sum_{r=1}^{M} \left[2W_r - W_{rs} + 3 \left(\delta(r > 1) + \theta_{r+1} - \theta_{r-1} \right) \varphi(R') \right] dX_r \quad , \tag{50}$$

and γ_r is now given by

$$\gamma_r = K \frac{m^{3/2} T^{5/2}}{p} \exp \left\{ - \frac{2W_r - W_{rs} + 3 \left(\delta(r > 1) + \theta_{r+1} - \theta_{r-1} \right) \varphi(R')}{kT} \right\} \tag{51}$$

where

$$K = (2\pi k)^{3/2} \frac{k}{h^3} \quad . \tag{52}$$

This is the only change in the adsorption isotherm as given by Eq. (21).

C. Solution and Discussion of the Adsorption Isotherm

The triangular site adsorption isotherm equations, as derived in the two previous subsections, cannot be solved exactly but must be solved iteratively. The iterative solution, which is called the exact theory, is summarized below where the superscript i is used to denote i-th iteration. The starting values for the iteration can be obtained from intelligent guesses or from the approximate theory which is also summarized below. The approximate theory can be solved exactly and is obtained by assuming that $X_r \ll S_r$.

1. Exact theory:

$$W_r^{(i)} = W_{rs} - 3\left[\delta(r > 1) + \theta_{r+1}^{(i-1)}\right]\varphi(R') + \theta_r^{(i-1)}\left[z(w) - 6\varphi(R)\right] +$$

$$+ \left[\theta_{r-1}^{(i)} + \theta_{r+1}^{(i-1)}\right]z(\delta) + \sum_{j=1}^{r-2}\theta_j^{(i)}z(a_r - a_j) + \sum_{j=r+2}^{M}\theta_j^{(i-1)}z(a_j - a_r) \quad , \qquad (53)$$

$$\gamma_r^{(i)} = K\frac{m^{3/2}T^{5/2}}{p}\exp\left\{-\frac{2W_r^{(i)} - W_{rs} + 3\left[\delta(r > 1) + \theta_{r+1}^{(i-1)} - \theta_{r-1}^{(i)}\right]\varphi(R')}{kT}\right\}, \qquad (54)$$

$$= \left[\frac{\theta_{r-1}^{(i)3} - \theta_r^{(i)}}{\theta_r^{(i)}}\right]\left[\frac{\theta_r^{(i)3}}{\theta_r^{(i)3} - \theta_{r+1}^{(i-1)}}\right]^{3\theta_r^{(i)2}} . \qquad (55)$$

The last equation is solved for $\theta_r^{(i)}$ by any standard iteration method.

2. Approximate theory (i=0):

$$W_r = W_{rs} - 3\delta(r > 1)\varphi(R') + \theta_{r-1}z(\delta) + \sum_{j=1}^{r-2}\theta_j z(a_r - a_j) \quad , \qquad (56)$$

$$\gamma_r = K\frac{m^{3/2}T^{5/2}}{p}\exp\left\{-\frac{2W_r - W_{rs} + 3\left[\delta(r > 1) - \theta_{r-1}\right]\varphi(R')}{kT}\right\} \quad , \qquad (57)$$

$$\theta_1 = \frac{1}{1+\gamma_1} , \quad \theta_r = \frac{\theta_{r-1}^3}{1+\gamma_r} \quad (r > 1) \quad . \qquad (58)$$

The approximate theory, which should be valid for monomolecular adsorption, has many interesting properties. For example, when

$$p \ll K m^{3/2} T^{5/2} \, ,$$

$$\theta_1 = \frac{p}{K m^{3/2} T^{5/2}} e^{\frac{W_1}{kT}} \, . \tag{59}$$

In other words, for low monomolecular coverage, the per cent coverage is directly proportional to the pressure. This linear dependence has been verified for Kr, A, and Ne on P33 carbon black.[20] In the range where Eq. (59) is invalid but only monomolecular adsorption is occurring, Eqs. (58) reduce to the conventional Langmiur adsorption isotherm for a single adsorbed layer. It is known that this particular adsorption isotherm fits many adsorption systems quite well. For the case where there are two adsorbed layers with $X_2 < S_2$, Eqs. (58) reduce to a superposition of two Langmiur adsorption isotherms - one for each layer. This superposition has been observed by Meyer[21] for helium on glass at 4.21°K. For three or more adsorbed layers, Eqs. (58) give a superposition of Langmiur type isotherms for each layer. However, for more than two adsorbed layers, the approximate theory appears to break down (see subsection D).

The exact theory is based on a solid state approach to the adsorbed layers and must become invalid for large r when the temperature is above the melting temperature of the adsorbate or if the resultant crystalline structure is neither face-centered cubic nor hexagonal close-packed. However, approximately 50 per cent of known materials crystallize in one of these two structures. Evidence[22] has been presented that helium actually does adsorb onto titanium dioxide as if it were in the solid state. This is logical since the added interaction energy due to the presence of the adsorbent is enough to place the adsorbed molecules in a potential field on the same order of magnitude as that present in the solid of the adsorbate. It is interesting to note that as r approaches 10^8, the exact theory should still be mathematically valid, and actually predict the properties of films several centimeters thick. The exact theory also predicts distinct steps in the adsorption isotherm as each layer is condensed (see subsection D). These distinct steps have not yet been satisfactorily verified by experiments and should be validated before the exact theory is applied to actual systems.

D. Numerical Results

The exact and approximate theories have been programmed for execution on an IBM 1620 Data Processing System. It is evident from the previous equations that this is the most logical method for obtaining numerical results. Assuming the ideal hexagonal close-packed structure $(R' = R)$ numerical results have been obtained for He and Ne on porous glass at 8.00°K, Ne on P33 carbon black at 8.00°K, and He on porous glass at 4.28°K.

Halsey[23] has measured the values of D and W_s for six different adsorbates on porous glass and eight adsorbates on P33 carbon black. Using his values and the Lennard-Jones (6-12) force constants, σ, ϵ, as given in Hirschfelder,[18] many of the various adsorption parameters can be obtained. Table III* lists the more interesting parameters for six adsorbates on porous glass. The values of W_s/k are quite high and demonstrate that adsorption is an important phenomenon - even for the inert gases. The values of W_ℓ/k as calculated from Eq. (43) agree very poorly with the measured values of W_ℓ/k . This was to be expected.

Using the parameters listed in Table III and a value of 0.022 for N_o, the approximate and exact theories were used to calculate the triangular site adsorption isotherm for He on porous glass at temperatures of 4.28° and 8.00°K. The results are plotted in Fig. 19 where "monolayer coverage" is defined as the ratio of the total number of adsorbed molecules and the number of sites present on the adsorbent, i.e., A/B . The approximate theory appears to be fairly good for $A/B < 3$ but fails badly for higher pressures. However, the most striking features of Fig. 19 are the very abrupt steps exhibited by the exact theory. These abrupt steps are even more striking when one examines the numerical data for 4.28°K. At a pressure of 1.966×10^{-36} atm., the first layer is only 3.34 per cent covered, whereas at a pressure of 1.967×10^{-36} atm., the first layer has a coverage of 99.95 per cent with no atoms in the second layer! This apparent condensation can be explained in the following manner. When a layer is filled to a certain threshold value, a very small rise in pressure will increase the coverage by a few tenths of a per cent. (This result is not new and is common to most adsorption isotherms.) However, from Eq. (42) it is seen that an increase of this magnitude significantly increases the adsorption energy which exponentially increases the coverage in that layer, which in turn increases the adsorption energy, etc. The result is a two dimensional condensation of each layer. This physically justifiable condensation will not occur in adsorption isotherms which neglect the intralayer intermolecular potentials.

---

* Due to a programming error the value of δ listed in the table is too large and should actually be slightly smaller than w . However, this error should not significantly alter any of the results herein.

TABLE III

VARIOUS ADSORPTION PARAMETERS FOR SIX ADSORBED GASES ON POROUS GLASS

| Adsorbate	σ_I (Å)	ϵ_I/k (°K)	g (Å)	ϵ/k (°K)	D (Å)	R (Å)	a (Å)	w (Å)	δ (Å)	σ_0 (Å^{-2})	W_ℓ/k (meas.) (°K)	W_ℓ/k (calc.) (°K)	W_s/k (°K)
He	2.178	681	2.556	10.22	1.87	2.869	2.343	4.849	7.156	0.140	10	37	342
Ne	2.248	1403	2.749	35.60	1.93	3.086	2.519	5.216	7.696	0.121	217	131	775
A	2.562	2324	3.405	119.80	2.20	3.822	3.121	6.460	9.532	0.079	784	439	1900
H$_2$	2.166	2006	2.928	37.00	1.86	3.287	2.683	5.555	8.197	0.107	54	136	992
N$_2$	2.318	3551	3.698	95.05	1.99	4.151	3.389	7.016	10.350	0.067	672	348	2150
O$_2$	2.201	3972	3.580	117.50	1.89	4.018	3.281	6.792	10.022	0.072	821	431	2060
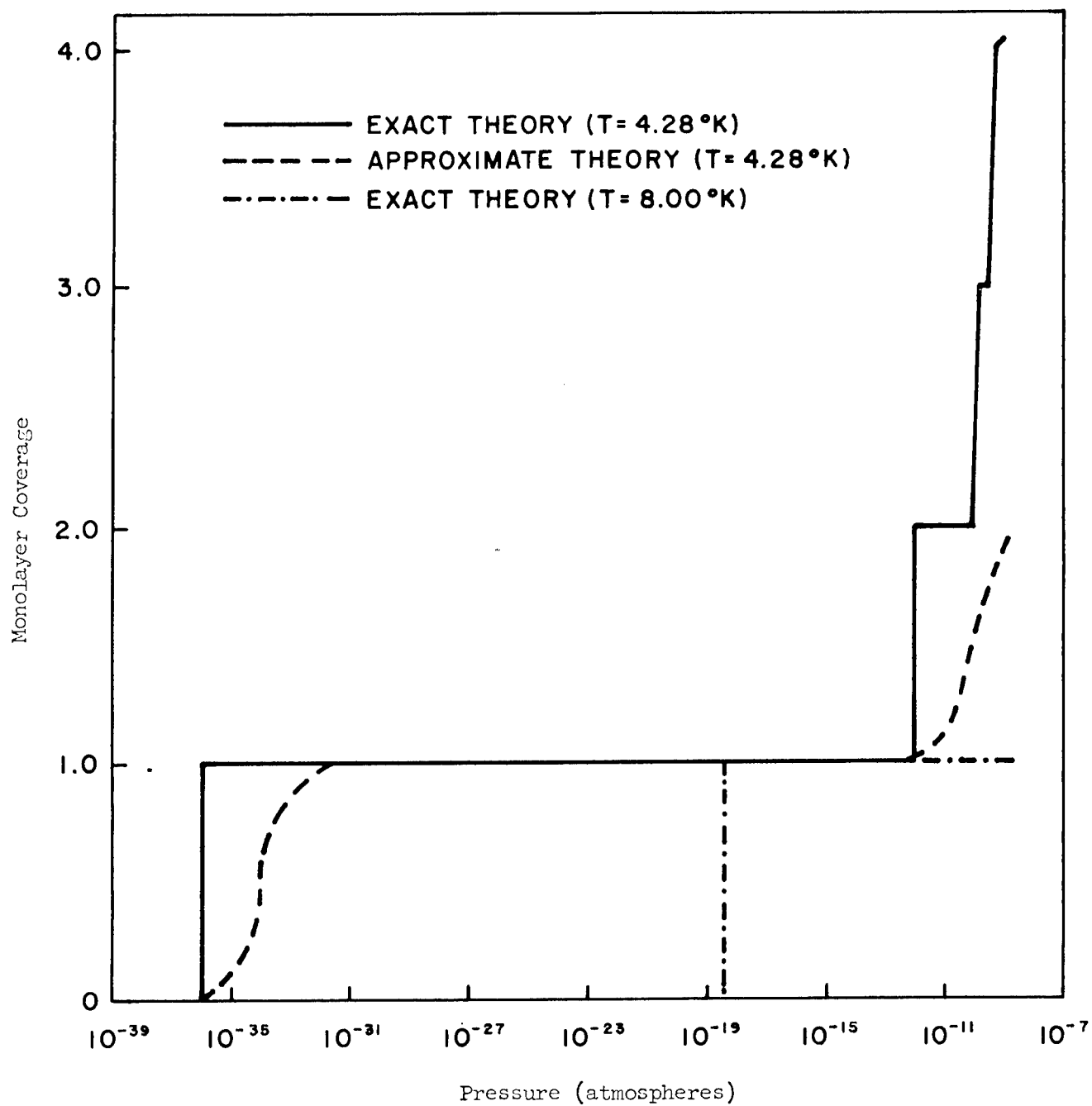
Fig. 19 - Triangular Site Adsorption Isotherms
for Helium on Porous Glass

The "effective" adsorption energy, E_r , is defined as

$$E_r = 2W_r - W_{rs} + 3\left[\delta(r > 1) + \theta_{r+1} - \theta_{r-1}\right]\varphi(R') \quad . \tag{60}$$

The effective adsorption energies for the first four layers of the above adsorption system at 4.28°K are plotted in Fig. 20. Again, the two-dimensional condensation of the adsorbate is seen to occur for one layer at a time. This condensation is undeniably present in the exact theory and provides an excellent criterion for the validity of the theory. However, caution must be exercised when attempting to experimentally detect these condensations since, at the higher pressures, the condensations may occur so frequently that the adsorption isotherm may appear to have a gradual slope.

To investigate the effect of the adsorbent, adsorption isotherms were calculated for neon on porous glass and on P33 carbon black at a temperature of 8.00°K. The isotherms are plotted in Fig. 21. It is evident that the P33 carbon black is the better adsorber. This may at first seem surprising since, according to Halsey,[23] the heat of vaporization of the first layer, at very low coverages, is higher on porous glass than on P33 carbon black. This is easily explained by looking at Fig. 22. Although the value of W_s for neon on porous glass is higher than the value of W_s for neon on P33 carbon black, the first layer on glass is closer to the surface than the first layer on P33. The result, as shown by the curves, is that the surface interaction energy falls off more rapidly above glass than above P33. The net result is that P33 carbon black is the better adsorber. Also shown in Fig. 22 are the curves for hydrogen and helium on porous glass. The result that glass adsorbs hydrogen more effectively than helium is not surprising.

Of the six adsorbates listed in Table III, helium, hydrogen, and nitrogen solidify in the hexagonal close-packed structure, whereas argon and neon solidify in the face-centered cubic structure. The crystal structure for solid oxygen is not definitely known. Since the computer calculations have been for the ideal hexagonal close-packed crystal structure, it is of interest to compare some of the calculated results for helium, hydrogen, and nitrogen with the results obtained from the true crystal structure of these three adsorbates.[24] This is done in Table IV where ρ_ℓ is the density of the liquid state in grams per cm^3, and the m and c subscripts refer to measured and calculated, respectively. The results for nitrogen are in very good agreement, whereas for hydrogen and helium the values of R as taken from Hirschfelder[18] appear to be too small. This agrees with Steele[25] who found that R = 3.7 Å for helium. Moreover, for argon on P33 carbon black, Sams[26] observed that the Lennard-Jones (6-12) force constants were changed by about 20 per cent from the gas-gas values.
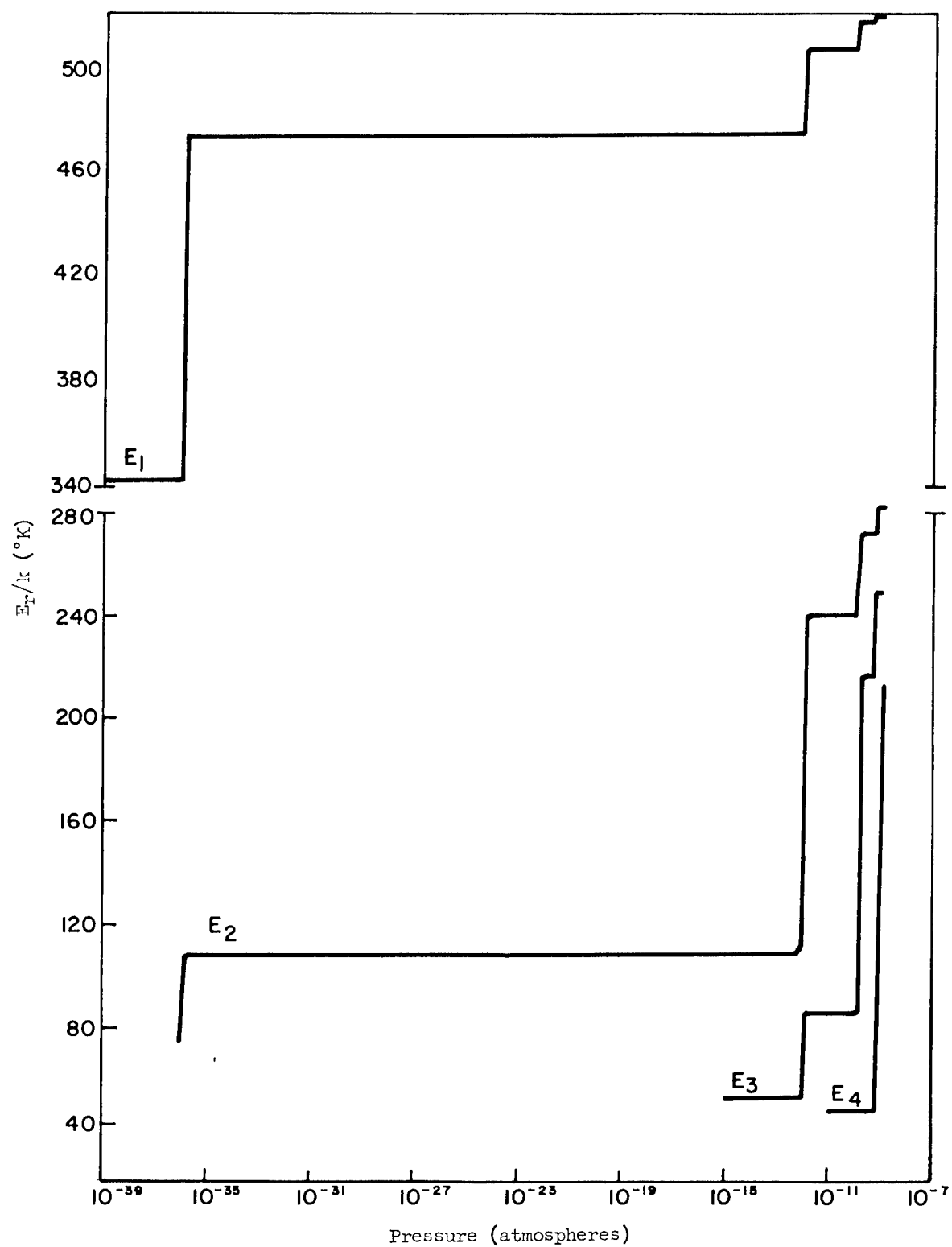
- 51 -

Fig. 20 - Effective Energies of Adsorption for Helium
on Porous Glass (T = 4.28°K)
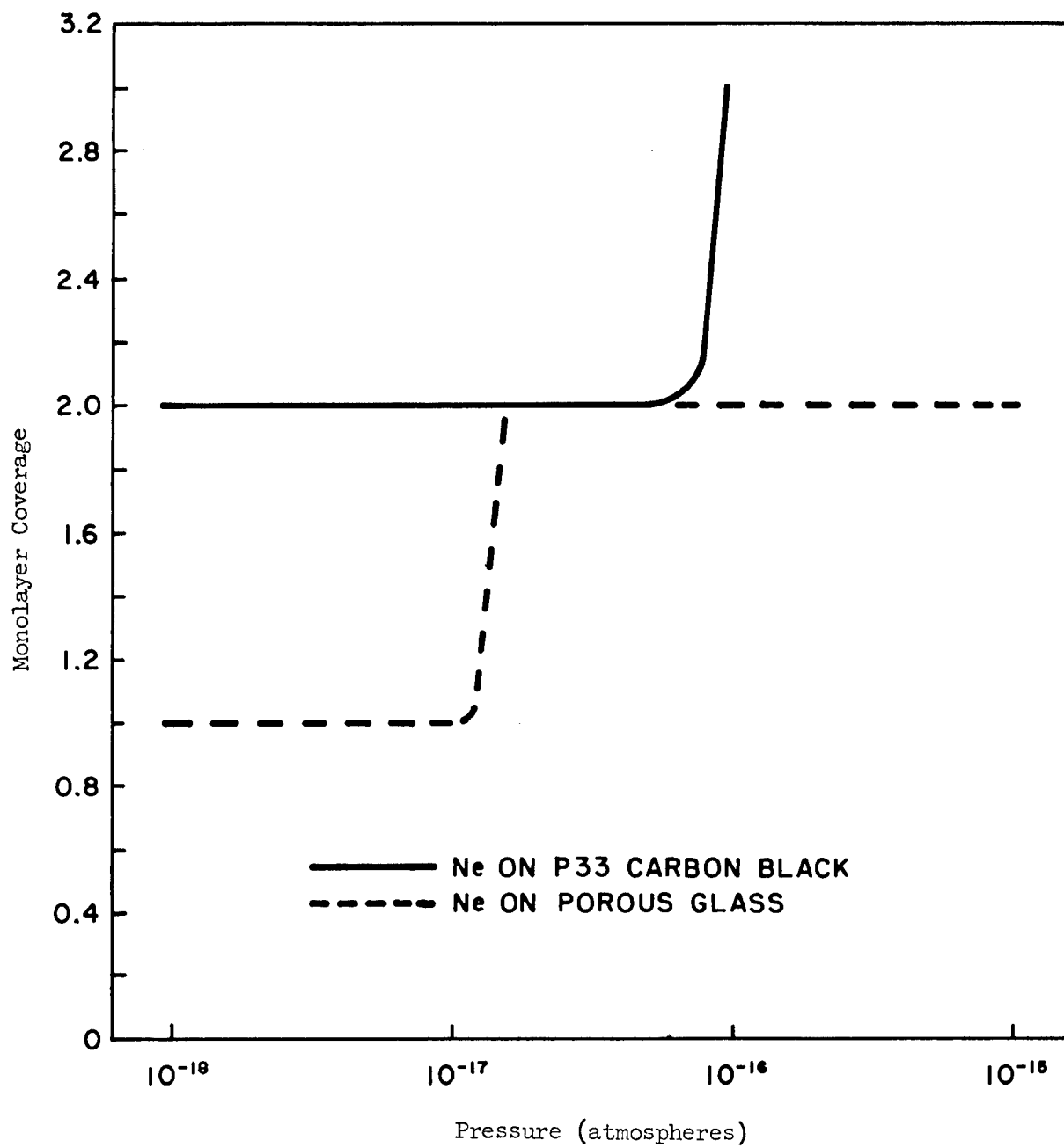
Fig. 21 - Triangular Site Adsorption Isotherms for Neon on Porous
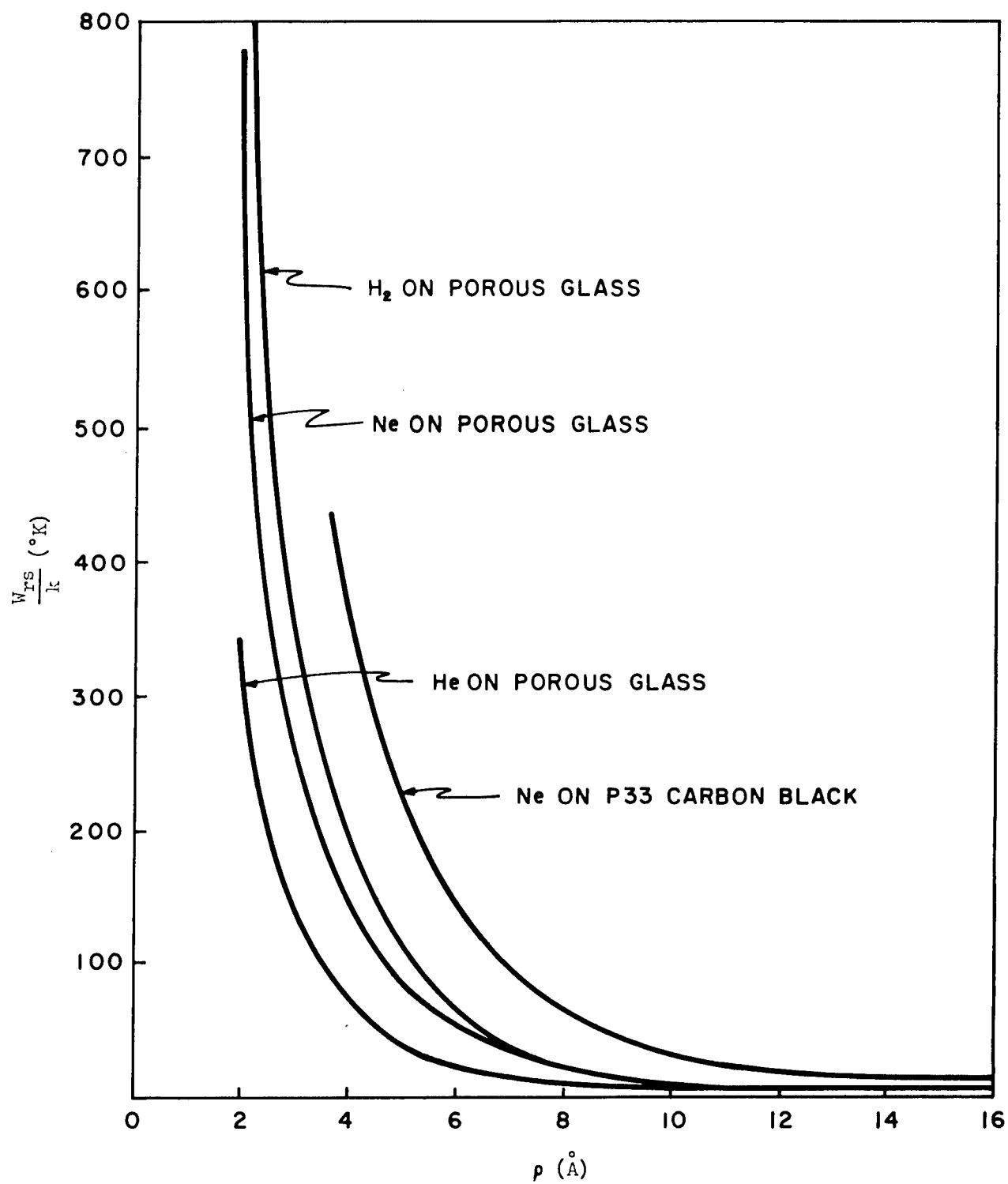Glass and P33 Carbon Black (T = 8.00°K)

Fig. 22 – Surface Interaction Energy as a Function of Distance From Surface

TABLE IV

COMPARISON BETWEEN CALCULATED AND MEASURED CRYSTAL STRUCTURES
FOR THREE ADSORBATES

Adsorbate	R_m (Å)	R_c (Å)	a_m (Å)	a_c (Å)	$(\rho_\ell)_m$ (g/cm^3)	$(\rho_\ell)_c$ (g/cm^3)
He	3.57	2.87	2.91	2.35	0.125	0.398
H$_2$	3.75	3.29	3.06	2.69	0.071	0.133
N	4.04	4.15	3.34	3.39	0.830	0.920

The main difficulty in using the triangular site adsorption isotherm
is in obtaining values of D and W_s for the adsorption systems of interest.
This difficulty is not insurmountable, however, since Halsey[23] has already
accomplished this for two adsorbents and eleven adsorbates. The Lennard-Jones
(6-12) force constants are well tabulated for most adsorbates[18] and present
no problem. Although, as shown in the previous paragraph, these force con-
stants may not be very accurate, they will undoubtedly suffice for the present.
Provided the theoretical isotherms presented here are experimentally verified,
the practical applications that result will be of significant value. For ex-
ample, consider a hypothetical case where an engineer is designing a glass
cryopanel to operate at a pressure of 10^{-10} atm. If, at a temperature of 8°K,
a cryopanel with a surface area of 4 m^2 is sufficient to do the particular job,
the curves in Fig. 19 show quite vividly that a cryopanel with a surface area
of 1 m^2 but operating at a temperature of 4.28°K would do a comparable job. In
other words, by decreasing the temperature by one-half, the required surface
area is decreased by one-fourth. The choice between these two possibilities
could then be based on economics. Another example of more scientific value is
to use the triangular site adsorption isotherm to investigate intermolecular
potentials, i.e., to determine k , ℓ , m , and n as molecules are more
closely packed when passing from the gas to the adsorbed state and from the
adsorbed to the solid state.

IV. DEVELOPMENT OF A TOTAL-PRESSURE GAUGE FOR
READINGS BELOW 10^{-12} TORR

Cold cathode magnetron gauges of a commercial type (NRC type 552 Redhead gauges) were chosen for this study. It was first noted that the extreme high vacuum system used for these experiments was capable of driving the magnetron gauges to cutoff, i.e., the low pressure at which a discharge can no longer be sustained. At this point it could be said that the tube has "fallen out of strike." The same tendency to cutoff may account for the break from a linear response at low pressures. The following sections describe the characteristics of the gauge and improvements affected by a cesiation treatment.

A. Discussion

A major source of electrons in the magnetron gauge is from gas molecule ionizations. The field emission current was deliberately made low to avoid the fixed background current which plagued the earlier Penning gauges. A disadvantage of the low field emission current is the reduced ability of the tube to strike at low pressures (striking time may be 10 or 15 min.).

An approach to both the striking and cutoff problems would be the addition of a pressure dependent source of electrons. It seemed feasible to obtain such a source of electrons from the cathode by lowering its work function so that impinging ions would cause electron emission. The additional electrons would be drawn through the recording ampmeter in the cathode circuit, thus raising the sensitivity of the gauge. In addition, the added electrons would help sustain the discharge.

Cesium metal could be deposited on the cathode of a magnetron tube to affect the desired reduction of work function and enhanced electron emission. However, it was feared that a cesium coating could cause a fixed photo-electron current background or permit heavy field emission to the anode. (The purpose of the intermediate auxiliary cathode is to prevent such field emission from the main cathode to the anode.) Field emission current would not be pressure dependent and could place a fixed lower limit on the gauge readings similar to the x-ray background effect.

Following a number of experimental treatments with cesium metal, it was determined that an undesirable fixed current, equivalent to a 2×10^{-10} Torr reading was produced by an excessive treatment with cesium. However, a normal or light treatment does not cause this detrimental effect and does produce advantageous results such as instantaneous striking and increased sensitivity (see subsection C below).

B. Experimental Technique

An extreme high vacuum system, which was specially designed to maintain an equilibrium flow rate of a known gas, was used for these experiments. The two magnetron gauges were separated by a known conductance so that a pressure ratio was established between them. A regulated flow of a suitable gas was introduced into the system so that the operating pressure could be varied.

Helium gas was chosen for these experiments for two reasons: (1) Pure helium gas with just 10 parts per million impurity may be obtained and admitted to a vacuum system through a vycor glass diffuser; and (2) helium will not be significantly adsorbed by the liquid nitrogen cold traps. Thus, the flow of pure helium was used to produce a reliable pressure differential between the two gauges. A wide range of pressure was covered from 10^{-6} Torr through 10^{-13} Torr and below (until the detection of ion current became unreliable) by varying the flow rate of helium through the diffuser.

Continuous plots of the two gauge outputs were recorded with a dual channel chart recorder. The plots show: the original gauge response; the point of break; and the new response curve. The pressure ratio between two gauges permitted a direct comparison of readings from the gauge above the break point (7×10^{-10} Torr for helium) to the gauge below the break. When the higher pressure gauge was at its break, the lower pressure gauge was indicating 6.5×10^{-11} Torr. Therefore, the ratio of readings was sufficiently large so that the higher pressure gauge readings remained in the linear response range while the lower pressure gauge readings dropped below the break. The arrangement of pressure ratios (between 5 and 100) was carefully chosen to insure reliable gauge comparisons.

Cesiation was accomplished by introducing cesium nitrate near the envelope of one gauge, then selectively baking that region of the vacuum system to 425°C under vacuum. (Cesium nitrate decomposes above 414°C.) A liquid nitrogen cold trap was maintained between the two gauges to limit the cesiation to one gauge only. A new sensitivity and response curve was then plotted for the cesiated gauge by direct comparison to the noncesiated gauge.

A cesiation treatment may be easily applied to a magnetron gauge by simply introducing a few grains of cesium nitrate into the system, then performing a normal vacuum bake-out to 425°C. In the results section below, the advantages and disadvantages of such a treatment are given.

C. Results

Figure 23 presents the typical results of a number of gauge comparison experiments. Curve 1 is a plot of the linear response of a Redhead cold cathode magnetron gauge (No. 1) operating above the break point. Curve 2 is a plot of the simultaneous response of a second Redhead gauge (No. 2) operating continuously at a pressure of one order of magnitude lower. This constant pressure differential is verified by the simultaneous readings of both gauges from 10^{-6} Torr down to 7×10^{-10} Torr (indicated for helium). The second gauge readings then break below the original curve and establish a new response Curve 3.

Curve 4 is a plot of the response from Gauge No. 2 after a "moderate" cesiation treatment. Gauge No. 1 has not been cesiated and the response still follows Curve No. 1. The actual pressure differential between the gauges is still an order of magnitude, but the sensitivity of Gauge No. 2 has apparently increased by a factor of two so that a continuous ratio of five to one is recorded from 10^{-6} Torr down to the same indicated break point. (However, the correction for sensitivity rise places the new break at one-half the pressure value of the previous break point.) The ion current-to-pressure response of this cesiated gauge then deviates from linearity and follows Curve 5 with a slope of 1.43. Corrections for the nonlinear response below 7×10^{-10} Torr (indicated) may be made by comparing vertical points on Curves 4 and 5.

The rise in sensitivity and corresponding lowering of the break were both anticipated benefits to be derived from a cesium treatment of the cathode. That is, the cesiation apparently did provide a beneficial source of electrons to sustain the magnetron discharge. These results are more indicative of the basic problem than they are useful since they vary with the degree of cesiation. One definite benefit of cesiation was the ability of the tubes to strike instantaneously even at pressures which produced ion currents of just 10^{-14} amp. The gauges retained this ability to strike instantly even after the sensitivity gain had been depleted.

The degree of sensitivity rise was found to depend upon the amount of cesiation treatment. A heavy treatment could raise the ion current response to 37 amp Torr (nearly an order of magnitude higher) but a fixed background current of 1.1×10^{-9} amp was produced. Therefore, a pressure limit of 2×10^{-10} Torr was imposed on the gauge even though the comparison gauge showed the pressure to be in the 10^{-13} Torr range. This background current did not exist in a light or "moderately" cesiated gauge. A heavily treated gauge could be reduced to the "moderate" level by merely rebaking the system.
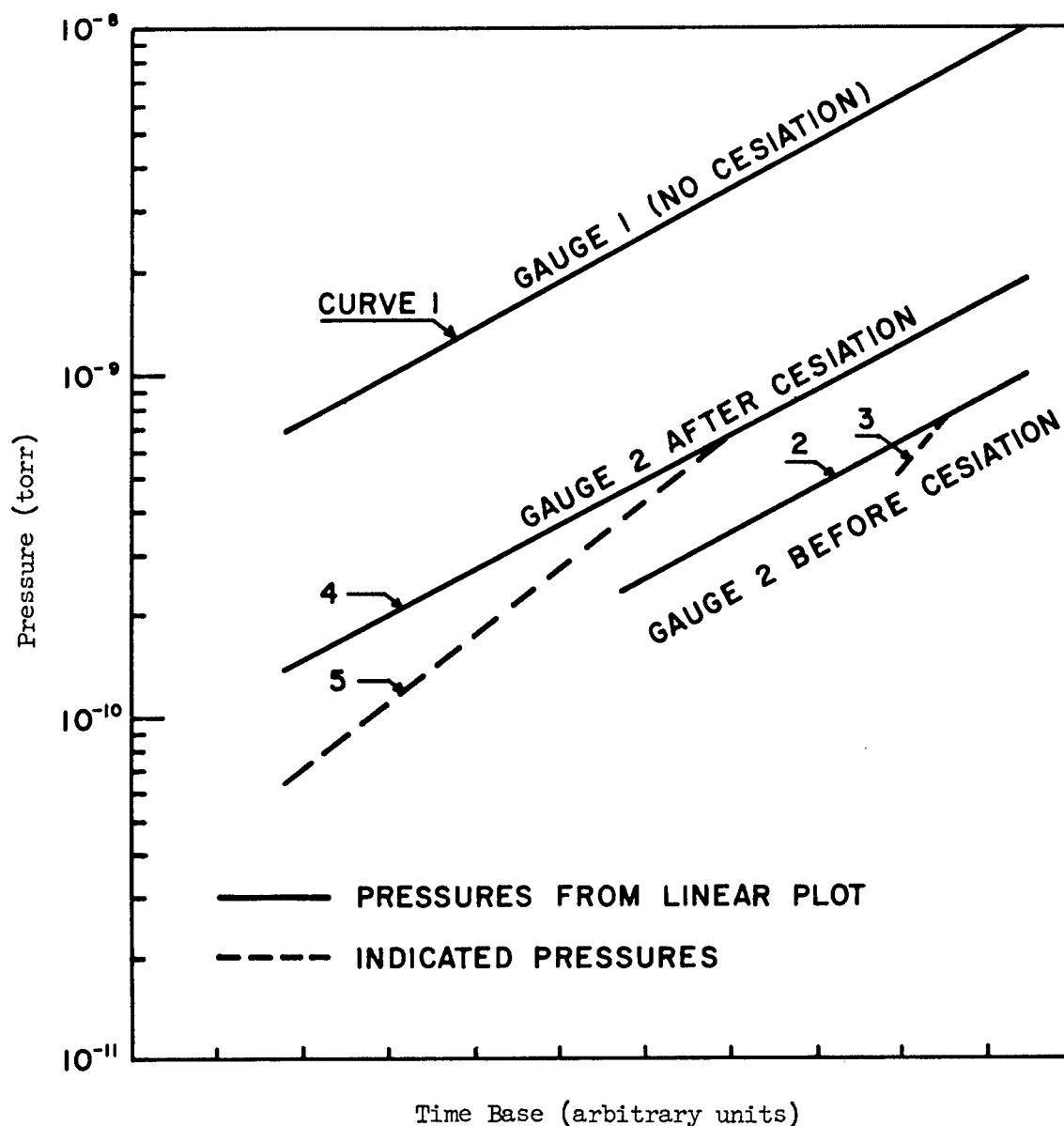
Fig. 23 - A Composite Graph of the Original Indicated Pressures for Helium,
From a Number of Redhead Gauge Comparison Tests (see p. 58). The
response of Gauge 1 (Curve 1) is taken as linear and used for com-
parison to draw Curves 2 and 4 from indicated pressure ratios. Gauge
2 follows Curve 2 for values above 7×10^{-10} Torr (3×10^{-9} amp), but
breaks from linearity below that point and establishes Curve 3. The
gauge response was raised to Curve 4 by cesiation (although the actual
pressure ratio remained constant) readings again followed linearity to
3×10^{-9} amp before the break to Curve 5. Correction for the in-
creased sensitivity shows that the break point was lowered by cesia-
tion to 3.5×10^{-10} Torr.

These results (p. 58) indicate that a magnetron gauge operation may be extended below 10^{-13} Torr. Additional observations and conclusions could be drawn from the data plots, but it is obvious that gauge comparisons and "calibrations" performed at these extremely low pressures will remain at best questionable until an absolute pressure standard is applied.

V. INVESTIGATION OF THE ADHESION OF METALS EXPOSED
TO VACUUM AND THERMAL OUTGASSING

Cold welding experiments were performed with metal samples commonly used in space vehicle construction: stainless steel (type 301 1/2 HD), aluminum alloy (X-2020-T6), and titanium alloy (6 per cent aluminum and 4 per cent vanadium).

The tests were arranged to duplicate the conditions to which these materials may be exposed in use: (1) combined thermal and vacuum degassing, or (2) vacuum exposure without thermal treatment (to simulate the case of metal parts shot directly into orbit). The latter condition was more difficult to simulate since the attainment of an ultra-high vacuum usually requires some bake-out procedure. A vacuum of 3×10^{-10} Torr, the equivalent of a 350 mile earth altitude, was attained without exposing the samples to bake-out; these tests were extended to 1,000 hr. duration. In another experiment, a pressure of 10^{-8} Torr (just within the UHV range) was maintained during thermal degassing at 350°C for 100 hr. duration. Chemical cleaning, thermal outgassing, and long term vacuum exposure were applied separately and in sequence to sample pairs with original surface texture and to samples with polished surfaces. The results of adhesion measurements performed first in air and following each of the treatments listed above were the same. That is, no increase of adhesion or cold welding resulted. The subsections A, B, and C below present a discussion of cold welding research in general, techniques developed here, and results obtained.

A. Discussion of Cold Welding Phenomena

It is known from the literature that some metals have shown the phenomena of sintering under elevated temperature. Also, bulk adhesion of metal surfaces may be observed for some ductile samples under deforming loads. That is, a threshold energy barrier may be overcome by adding thermal energy either directly or by heavy compressive loading. The loading may serve another necessary purpose toward achieving full bulk adhesion, i.e., plastic deformation of the surfaces to render a large area of contact. For practical structural materials, with the normal amount of surface roughness, such loading above the deformation level appears to be a necessary ingredient for a significant "cold welding" effect. However, there have been indications of seizure reported between moving metal parts with low level loading in a vacuum environment. In these cases abrasive action may be a necessary ingredient resulting in removal of oxides and other contaminants and by the promotion of asperity welding.

The phenomenon of cohesion of clean atomically smooth surfaces has been demonstrated for lamellar silicate minerals.[27/] Mica crystals were cleaved along the basal plane in an ultra-high vacuum of 10^{-13} Torr, then allowed to reheal by a touch contact, without interfacial loading. The molecularly smooth and clean surfaces re-established cohesion to 87 per cent of the original bulk crystal value.[27/] This result indicates that clean surfaces with a large real area of contact may be expected to cohere if the net free energy[28/] of the pair is lowered by the formation of an interface. The latter condition has been shown[29/] to exist theoretically for mica, as may be readily visualized from the ionic bonding scheme, i.e., the attractive charge distribution on cleaved layers of mica[29/] assures a reduction of free surface energy as the layers pull back together.

The results of previous experiments such as the one just mentioned have contributed some understanding of the cold welding phenomena. Now an important problem remains to be answered: will ordinary structural materials with oxide layers and normal surface roughnesses and under the conditions of a vacuum environment, exhibit cold welding? The negative answer obtained here (see section C below) seems to be in agreement with the criterion of free energy change.[28/] The metal surfaces with stable oxides would not be expected to experience a lowering of free surface energy when brought into contact. In addition, the surface roughness of even the polished samples would prevent large area contact, so that cold welding was neither expected nor observed for the metal samples and the simulated conditions of practical use applied in this study.

B. <u>Equipment and Techniques</u>

1. <u>Metal samples for cold welding tests:</u> Samples were formed for adhesion studies from three structural materials: stainless steel (type 301 1/2 HD), aluminum (X-2020-T6) and titanium alloy (6 per cent aluminum and 4 per cent vanadium). The sets of sample pairs were cut from the same large plates as used in construction of some space vehicles.

The 1 cm.^{2} surface areas chosen were, of course, free of unusual defects such as abrasion marks. For some samples the original surface texture was left unaltered while the surface of other samples was mechanically polished. All samples were chemically cleaned to remove dirt and oils.

Sample dimensions were as follows: contact faces of 1.0 cm. x 1.0 cm., thickness 0.25 cm., reverse side face on one sample of each pair is 1.0 cm. x 1.2 cm. The tapered edges of the one sample permit glass clamps to hold that piece rigid while the other member of the pair is free to move (see Fig. 24).
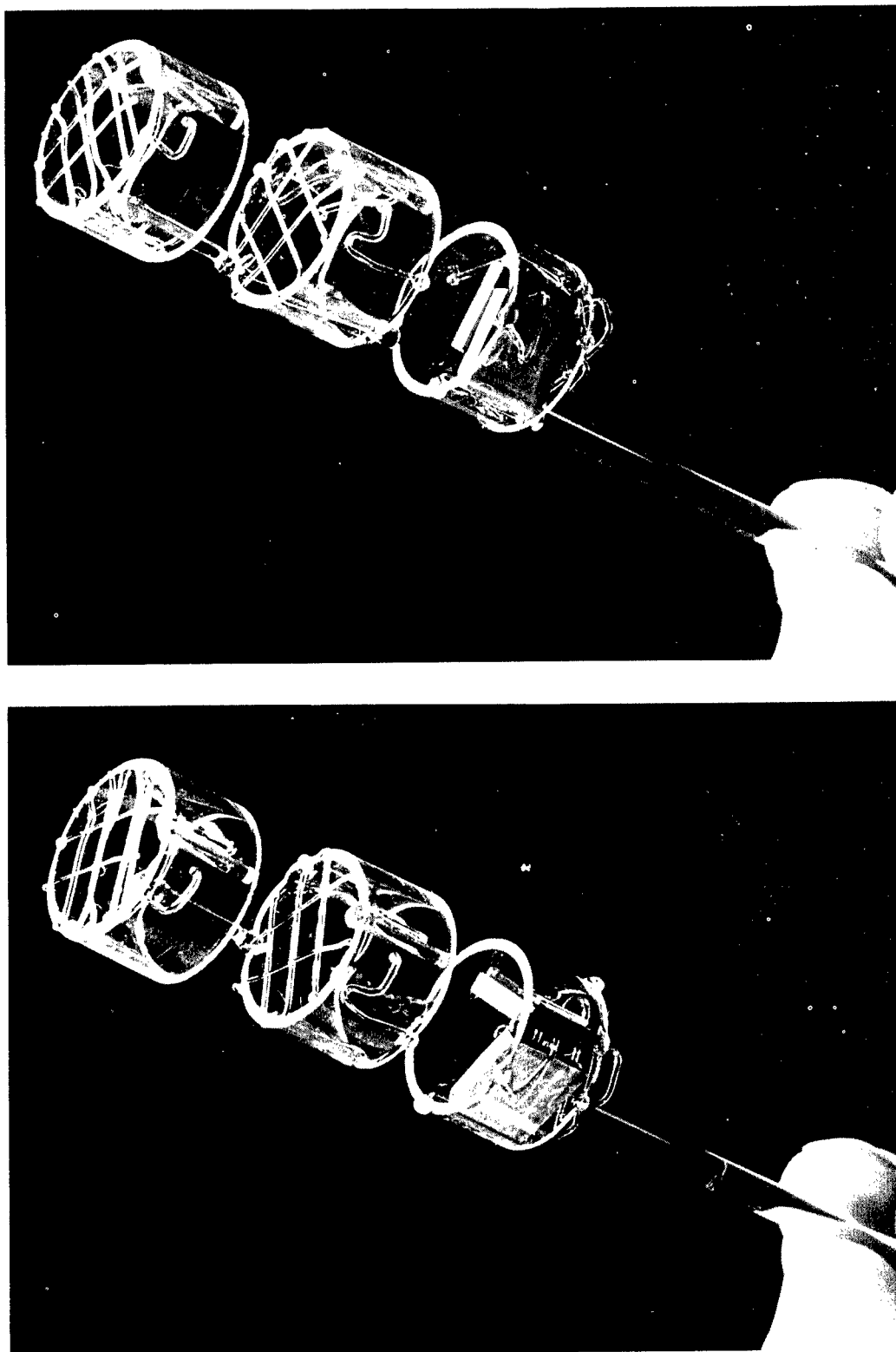
P 6 4

Fig. 24 – Glass Sample Holder for Adhesion Studies in Vacuum. Glass Supports are Designed to Avoid Adhesion Between Rigid Parts of the Glass and Metal, Thus Permitting Thermal Expansion. Samples may be Alternately Exposed to Vacuum and Brought Into Contact for Adhesion Tests.

The glass support members were designed to accommodate thermal expansion of the metal samples. Two samples of each material listed above were mounted as pairs with their faces exposed for vacuum outgassing. The tube, containing the sample pairs, may be rotated so that the free samples fall onto the fixed members with a 1 cm.^{2} interface (Fig. 24). Continued rotation provides a measure of adhesion between the free and fixed samples in terms of the maximum angle of repose. The interfacial surfaces may again be opened for vacuum outgassing by rotating the tube to its original position.

2. Redhead gauges used as vacuum pumps: Cold cathode magnetron ionization tubes (NRC Type 552 Redhead gauges) were employed as both pressure measuring devices and vacuum pumps. The gauge ionizes gas molecules then accelerates them through a 6,000 v. potential to the cathode. The current flow gives a measure of pressure while the physical burial of ions in the cathode provides a pumping action.

The ionization efficiency and effective volume of a Redhead gauge is high compared to that of a Bayard-Alpert type gauge; also the accelerating potential is 200 times greater, thus increasing the effective burial of ions. Since Bayard-Alpert gauges have been successfully used as pumps with a speed of 0.04 liter/sec it is apparent that Redhead gauges should be at least 25 times more efficient with a speed of 1 liter/sec (for nitrogen).

A 6,000-v. power supply was adapted to simultaneously provide the anode potential for a number of Redhead tubes (see Fig. 25). The tubes may be operated indefinitely with only this voltage source and permanent magnets. Pressures may be monitored at any time by connecting a control unit (NRC model 752) to each tube alternately. This arrangement provides for inexpensive long-term tests of the effects of an ultra-high vacuum environment.

3. Getter-ion pumps used for outgassing and for a movable system: A UHV system was constructed to process the magnetron tubes prior to seal-off. Figure 26 shows two tubes mounted for bake-out. The tubes are connected through glass seal-offs of high conductance. This auxiliary vacuum system is also used to rigorously outgas component parts, such as the helium permeation chamber, before attaching to the partial pressure analyzer system.

Another UHV system, similar to that of Fig. 26, was mounted on a rotation axis for cold welding tests. The portable nature of the getter-ion pump was used to advantage by simply removing the heavy magnet and high voltage lead, then rotating the entire system (see Fig. 27) until the sample pairs fell together and then reached the maximum angle of repose. A reverse rotation, with the getter-ion pump passing through a slot in the table, caused the samples to fall apart for continued vacuum exposure.
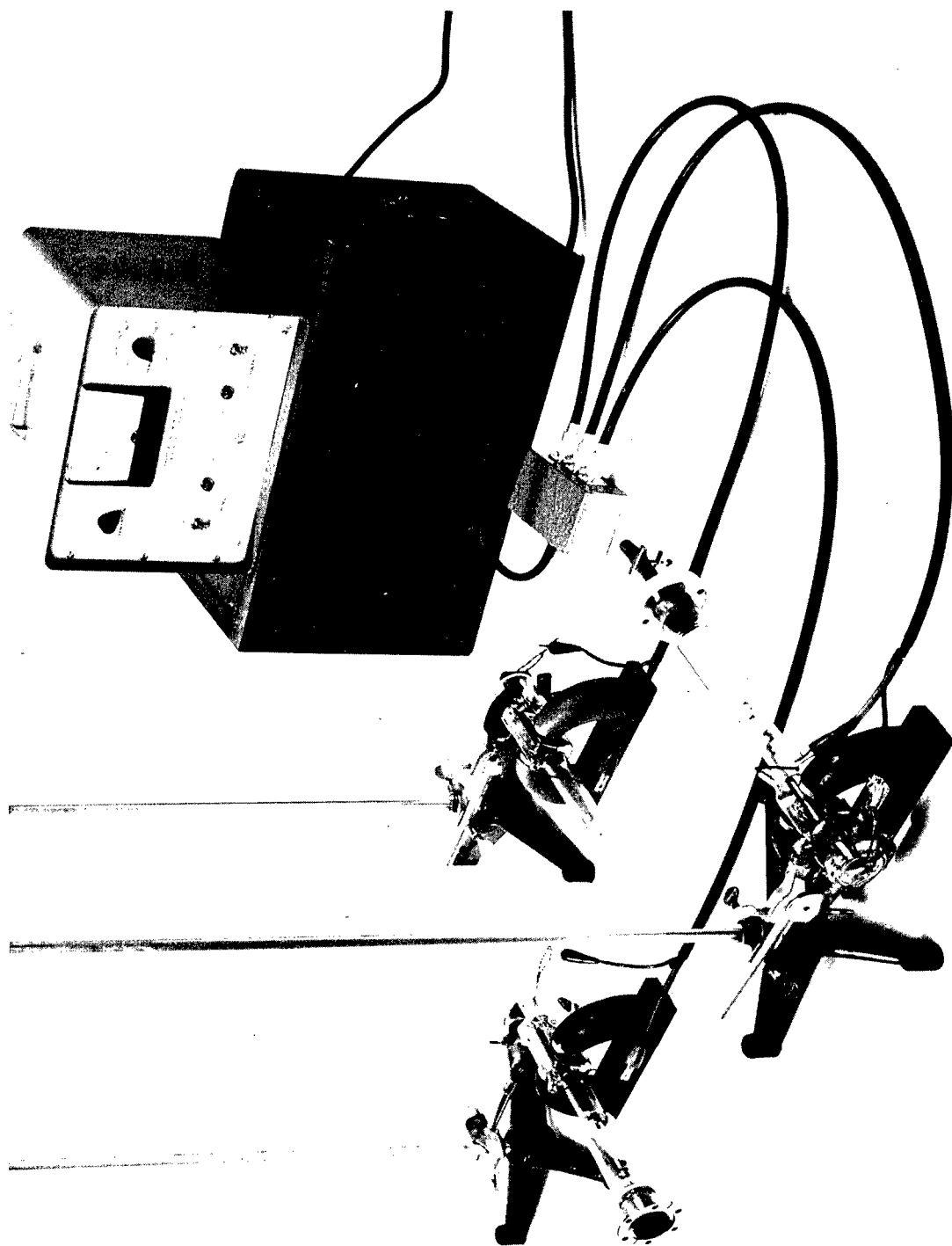
Fig. 25 - Three Magnetron Vacuum Systems may be Mounted for Long-Term Experiments as Indicated. One 6,000-v. Power Supply Will Operate a Number of Systems for Indefinite Periods.
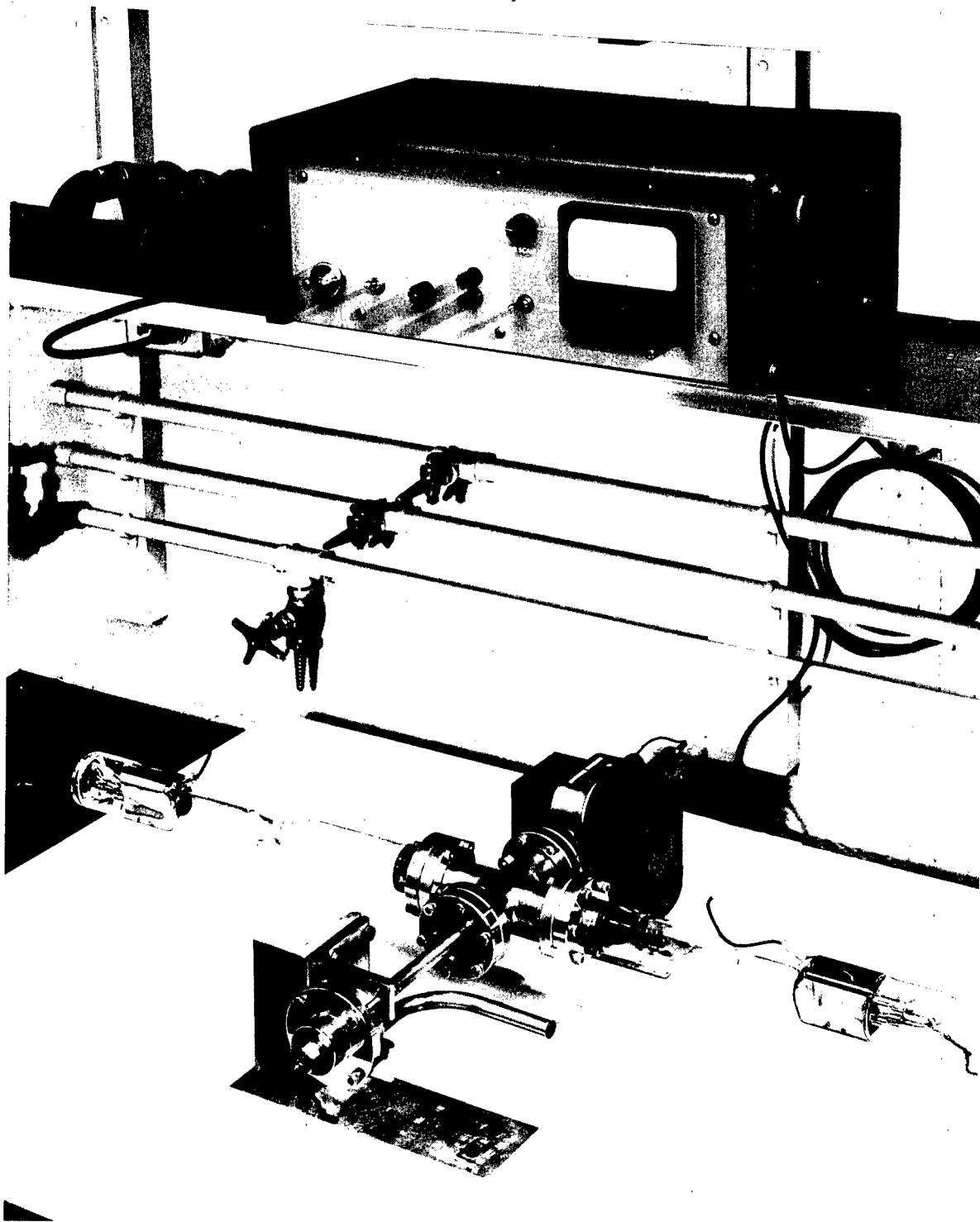
Fig. 26 - Auxiliary Vacuum System for Long-Term Degassing and Preparation of
Experiments for the Analyzer System (Fig. 12). Two Magnetron
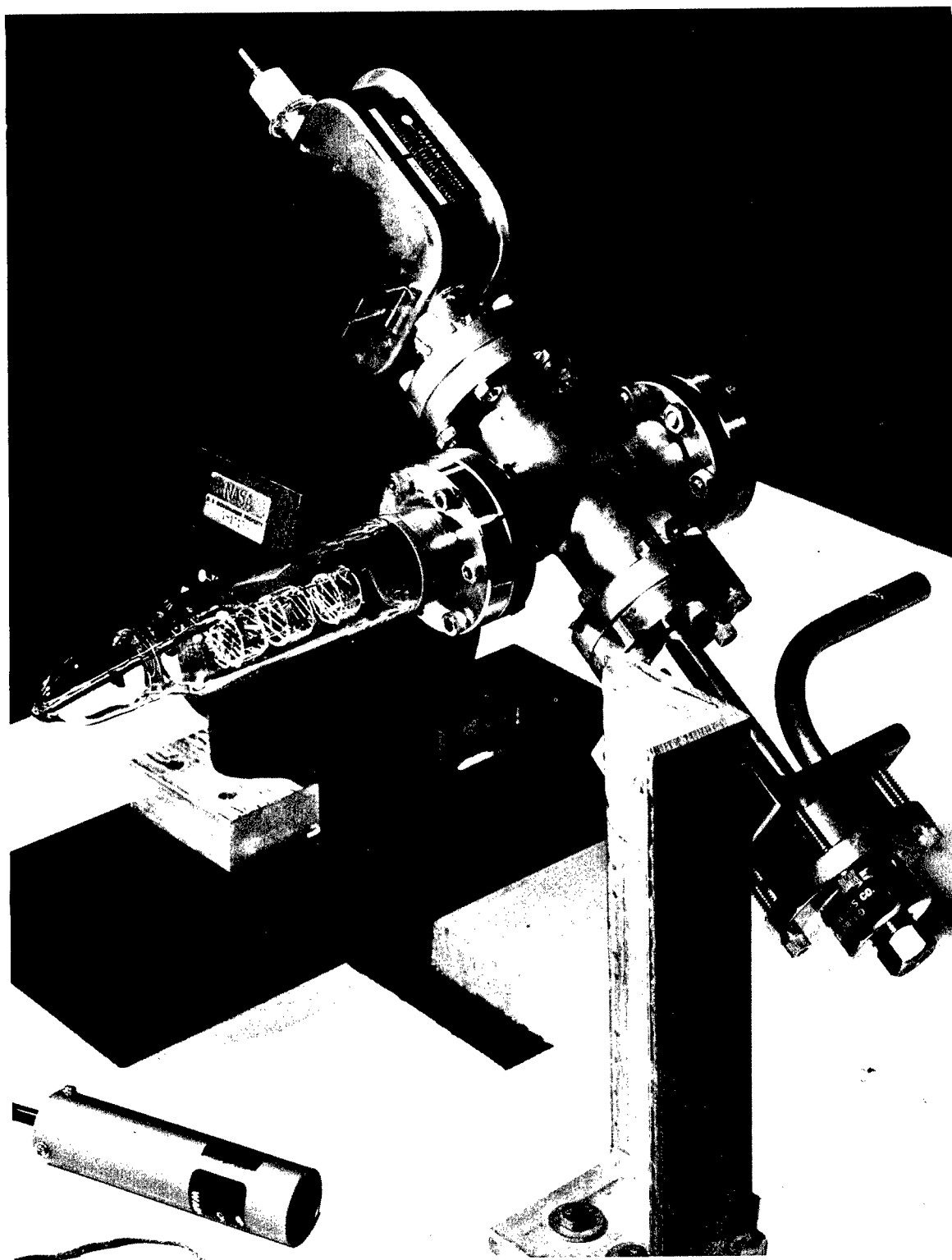Tubes Are Mounted for Bakeout Prior to Glass Seal-Off.

Fig. 27 - A UHV System for Cold Welding Tests in Which the Portable Nature
of the Getter-Ion Pump Permits Sample Manipulation (see p.
64) via Gravitational Force. A Machine Bolt Serves as
the Rotation Axis for the System.

C. Results of Cold Welding Tests

Cold welding experiments have been performed under various related conditions of vacuum, time, and temperature. Adhesion tests were performed at each step of the experiments: before evacuation, after long-term exposure to ultra-high vacuum, and following bake-out. Each of these measurements showed that no increase of adhesion occurred between the metal samples as a result of either thermal degassing or long-term exposure to vacuum environment.

The quantitative results for the aluminum, titanium, and stainless steel samples with original surface textures were as follows: (1) after chemical cleaning, the maximum angle of repose measured in air was 28°; (2) following exposure to a high vacuum of 5×10^{-8} Torr for 500 hr. the angle of repose still measured 28°; (3) following a 100 hr. bake at 350°C under a 5×10^{-8} Torr vacuum the angle was again 28°.

Aluminum, titanium, and stainless steel samples with polished faces gave the following results: (1) the maximum angle of repose between the samples in air was 21°; (2) during exposure to an ultra-high vacuum of 3×10^{-10} Torr the angle varied randomly between 20 and 23°, but the average remained approximately the same for exposures of 100, 500 and 1,000 hr; (3) following a combined thermal-vacuum degassing at 350°C and 10^{-8} Torr for 100 hr. the maximum angle of repose still averaged 21° indicating that no change of adhesion resulted from any of these vacuum treatments.

p 69

1. Bryant, P. J., and C. M. Gosselin, UHV Controlled Atmosphere Test Chamber Using Mercury Vapor Pump Sets, 1224-1227, 1961 Trans. of the Eighth Vacuum Symposium and Second International Congress, Pergamon Press (1962).

2. Venema, A., "The Production of Ultra-High Vacua by Means of a Diffusion Pump," Vacuum, 9, 1, 54-57 (1959).

3. Dushman, S., and J. M. Lafferty, Scientific Foundations of Vacuum Technique, Second Edition, Chapter 3.

4. Alexander, Paul, J. of Sci. Instr., 23, pp. 11-16, January, 1946.

5. Riddiford, L., and R. F. Coe, J. of Sci. Instr., 31, pp. 33-36, February, 1954.

6. Ho, T. L., Physics, 2, pp. 386-395, May, 1932.

7. Fujinaga, A., and T. Hiroshi, 1962 Trans. of the Ninth Vacuum Symposium, pp. 390-94 (1962).

8. Dayton, B. B., Review of Sci. Instr., 19, pp. 793-804, November, 1948.

9. Dushman, S., and J. M. Lafferty, Scientific Foundations of Vacuum Technique, Second Edition, pp. 93-95 (1962).

10. Davis, W., and T. Vanderslice, 1960 Trans. of Seventh Vacuum Symposium, 417-420, Pergamon Press, New York (1961).

11. Davis, W. D., 1962 Trans. of the Ninth Vacuum Symposium, 363-370, Macmillan Press (1963).

12. Biondi, M. A., 1960 Transactions of the Seventh National Vacuum Symposium, Pergamon Press (London) pp. 24-28 (1960).

13. Lichtman, David, private communication.

14. Hablanian, M. H., and P. L. Vitkus, Residual Gases in Ultra-High Vacuum Systems with Oil Diffusion Pumps, Tenth National Vacuum Symposium (1963) 140-145, Macmillan, New York.

15. Brunauer, S., P. H. Emmett, and E. Teller, J. of Amer. Chem. Soc., 60, 309 (1938).

REFERENCES (Concluded)

16. Halsey, George, J. of Chem. Physics, 16, 10, p. 931, October, 1948.

17. Band, William C., Introduction to Quantum Statistics, D. Van Nostrand Company, Inc. (1955).

18. Hirschfelder, Joseph, Charles Curtiss, and Byron Bird, Molecular Theory of Gases and Liquids, John Wiley & Sons, Inc. (1954).

19. Sproull, W. T., X-Rays in Practice, McGraw-Hill, p. 313 (1946).

20. Constabaris, G., J. H. Singleton, and G. D. Halsey, Jr., J. Phys. Chem., 63, 1350 (1959).

21. Meyer, L., Phys. Rev., 103, 6, 1593 (1956).

22. Aston, J. G., S. V. R. Mastrangelo, and R. J. Tykodi, J. Chem. Phys., 23, 9, 1633 (1955).

23. Halsey, G. D., Jr., 1961 Trans. of the Eighth Vacuum Symposium and Second International Congress, 119, Pergamon Press (1962).

24. American Institute of Physics Handbook (1963).

25. Steele, W., Jr., J. Chem. Phys., 25, 819 (1956).

26. Sams, J. R., G. Constabaris, and G. D. Halsey, Jr., J. Chem. Phys., 36, 5, 1334 (1962).

27. Bryant, P. J., Cohesion of Clean Surfaces and the Effect of Adsorbed Gases, 1962 Trans. of the Ninth Vacuum Symposium, Macmillan Press (1962).

28. Spalvins, T., and D. V. Keller, Adhesion Between Atomically Clean Metallic Surfaces, 1962 Proceed. American Vacuum Soc. Metallurgy Division Conf.

29. Bryant, P. J., L. H. Taylor, and P. L. Gutshall, Cleavage Studies of Lamellar Solids in Various Gas Environments, 1963 Trans. of the Tenth Vacuum Symposium, McGregor Werner Press (1963).

NASA SCIENTIFIC AND TECHNICAL PUBLICATIONS

TECHNICAL REPORTS: Scientific and technical information considered important, complete, and a lasting contribution to existing knowledge.

TECHNICAL NOTES: Information less broad in scope but nevertheless of importance as a contribution to existing knowledge.

TECHNICAL MEMORANDUMS: Information receiving limited distribution because of preliminary data, security classification, or other reasons.

CONTRACTOR REPORTS: Technical information generated in connection with a NASA contract or grant and released under NASA auspices.

TECHNICAL TRANSLATIONS: Information published in a foreign language considered to merit NASA distribution in English.

TECHNICAL REPRINTS: Information derived from NASA activities and initially published in the form of journal articles.

SPECIAL PUBLICATIONS: Information derived from or of value to NASA activities but not necessarily reporting the results of individual NASA-programmed scientific efforts. Publications include conference proceedings, monographs, data compilations, handbooks, sourcebooks, and special bibliographies.

Details on the availability of these publications may be obtained from:

SCIENTIFIC AND TECHNICAL INFORMATION DIVISION

NATIONAL AERONAUTICS AND SPACE ADMINISTRATION

Washington, D.C. 20546